Advancing Electrochemical Modelling of PEM Electrolyzers through Robust Parameter Estimation with the Weighted Mean of Vectors Algorithm

Hossam Ashraf[1*], Eiji Kawai[1], Masahiro Mae[1], and Ryuji Matsuhashi[1]

[1] Department of Electrical Engineering and Information Systems, The University of Tokyo, Tokyo 113-8656, Japan.

[*]Corresponding author
✉ Email: hossam-ashraf@g.ecc.u-tokyo.ac.jp, ekawai@g.ecc.u-tokyo.ac.jp, mmae@g.ecc.u-tokyo.ac.jp, matu@g.ecc.u-tokyo.ac.jp

Graphical abstract-

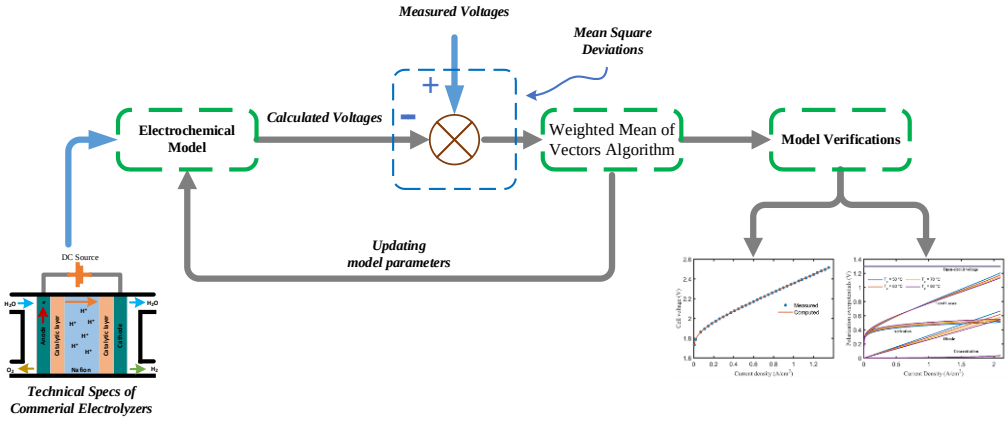

Abstract- The electrochemical modelling of proton exchange membrane electrolyzers (PEMEZs) relies on the precise determination of several unknown parameters. Achieving this accuracy requires addressing a challenging optimization problem characterized by nonlinearity, multimodality, and multiple interdependent variables. Thus, a novel approach for determining the unknown parameters of a detailed PEMEZ electrochemical model is proposed using the weighted mean of vectors algorithm (WMVA). An objective function based on mean square deviation (MSD) is proposed to quantify the difference between experimental and estimated voltages. Practical validation was carried out on three commercial PEMEZ stacks from different manufacturers (Giner Electrochemical Systems and HGenerators™). The first two stacks were tested under two distinct pressure-temperature settings, yielding five V–J data sets in total for assessing the WMVA-based model. The results demonstrate that WMVA outperforms all optimizers, achieving MSDs of 1.73366e-06, 1.91934e-06, 1.09306e-05, 6.18248e-05, and 4.41586e-06, corresponding to improvements of approximately 88%, 82.9%, 82.4%, 54.5%, and 59.5% over the poorest-performing algorithm in each case, respectively. Moreover, comparative analyses, statistical studies, and convergence curves confirm the robustness and reliability of the proposed optimizer. Additionally, the effects of temperature and hydrogen pressure variations on the electrical and physical steady-state performance of the PEMEZ are carefully investigated. The findings are further reinforced by a dynamic simulation that illustrates the impact of temperature and

supplied current on hydrogen production. Accordingly, the article facilitates better PEMEZ modelling and optimizing hydrogen production performance across various operating conditions.

Keywords: Green hydrogen; Proton exchange membrane electrolyzer; Electrochemical model; Polarization losses; Voltage efficiency.

1. Introduction

1.1. Motivation

Due to the increasing need for power and the decreasing supply of fossil fuels, the search for green energy alternatives has become critical [1]. The persistent consumption of fossil fuels has been releasing huge amount of greenhouse gasses leading to a range of ecological issues [2]. Accordingly, renewable energy sources (RESs) are at the forefront of current energy investments due to their reliance on clean and sustainable resources such as solar, wind, geothermal, and hydropower [3]. In this regard, some countries have adopted a zero-carbon strategy to be achieved by 2050, which refer to assigning RESs as the primary and sole energy sources for all residential, commercial, industrial sectors [4].

Hydrogen plays a vital role in this RESs transformation. It possesses unique technical characteristics that make it an effective and adaptable energy carrier. For example, hydrogen has an energy density per kilogram nearly three times that of gasoline. Moreover, hydrogen can be stored as a compressed gas, cryogenically as a liquid, or bound within chemical compounds [5]. Such storage flexibility offers an adequacy to various applications and configurations [6]. However, its low volumetric energy density requires high-pressure storage. Particularly, green hydrogen is the most sustainable hydrogen-generation form, typically via water electrolysis. Such process occurs using an electrolyzer (EZ) powered by solar, wind, or other RESs, resulting in zero carbon emissions throughout the production process [7].

Practically, an EZ incorporates a process that splits water into hydrogen and oxygen using electrical energy. It consists of two main electrodes, an anode and a cathode, separated by an electrolyte [8]. When an electric current flows through the electrodes, water molecules at the anode are oxidized, releasing oxygen gas and positively charged hydrogen ions (protons) or oxide ions, depending on the EZ type. These ions then move through the electrolyte to the cathode, where they are reduced to form hydrogen gas. For instance, proton exchange membrane EZs (PEMEZs) use a proton-conducting membrane that allows only protons to pass through, while alkaline EZs (AEZs) use an alkaline solution as the electrolyte to facilitate ion transport [9].

Specifically, PEMEZs were initially developed to tackle the operation issues of AEZs in terms of restricted operation range and low current density [10]. Their rapid dynamics, low-temperature operation, compactness, and modularity make them ideal for stabilizing fluctuating renewable inputs [11]. Such popularity highlights how important precise modelling of PEMEZ is. It enables operators to analyse, evaluate, control, and optimize PEMEZ performance over several simulated operating scenarios before deploying physical setups. This would save the high costs associated with trial-and-error adjustments in hardware [12].

1.2. Literature review

Recently, numerous efforts have been devoted to capturing the electrical behaviour (V–J curve) of PEMEZs through mathematical models [13].

1.2.1. Equivalent-circuit and empirical models

For example, an equivalent circuit model is presented in [14] which correlates the current density to the applied voltage at certain pressure and temperature. The authors in [15] introduced an electrical model to simulate the dynamic response of PEMEZ due to a step change in the drawn current. Their model comprises a voltage source, resistance, and capacitance. However, both models fail to address how physical and chemical factors, such as water content and electrolysis rate, could influence the electrical performance.

Another attempt to imitate PEMEZ dynamic performance over variable temperatures and pressures is presented in [16]. Moreover, the behaviour of each individual polarization losses is also described highlighting that the ohmic losses share the largest effect on the EZ performance. A parametric model was developed in [17] that can simulate EZ performance under different flow rates, pressures, temperatures, and gas production. On the other hand, the researchers in [18] derived a mathematical formation to assess PEMEZ behaviour with respect to varying current density, membrane thickness, cathode pressure, and temperature. Furthermore, a hardware-in-the-loop simulation was implemented [19] to experimentally validate the outcomes of the proposed mathematical model.

1.2.2. Electrochemical modelling

Principally, electrochemical models account for both chemical factors, such as electrolysis rate, water content, and physical factors, such as membrane thickness, cell area, to predict the V–J behaviour more faithfully [20]. In this context, an empirical and a semi-empirical temperature-dependent model were first proposed for an AEZ cell in [21], and subsequently adapted to PEMEZs in [22]. That detailed formulation was further enhanced in [23] to capture temperature and pressure effects, but it relies on eight empirical coefficients that are not provided by manufacturers. Moreover, the identification of such empirical coefficients doesn’t guarantee a full characterization of the PEMEZ chemical features.

A basic thermodynamic circuit models the PEMEZ as a single voltage source, representing the minimum energy for electrolysis, but it neglects ohmic resistance as well as activation and concentration overpotentials [24]. Thus, the authors in [25] developed a detailed electrochemical model that covers all the aforementioned losses for practical simulation of the EZ nonlinearity throughout the full-range operation. However, this model depends on several empirical parameters not provided by manufacturers. So, their accurate estimation is essential for dependable PEMEZ simulation, control, and performance forecasting.

1.2.3. Role of optimization approaches

In this context, several estimation techniques have been employed in the literature to identify model parameters. Such techniques are generally categorized into numerical and metaheuristic approaches. Example of numerical-based approaches exist in [15, 25-27]. Particularly, a Taguchi design was applied in [25] to tune operating pressures and temperatures as well as membrane thickness, water content, and anode/cathode exchange current densities. The least squares regression technique, employed in [15], identified a mix of static and dynamic parameters, whereas Gauss–Newton optimization, implemented in [26], minimized a nonlinear least quadratic error to extract five key coefficients (maximum current density, exchange current density, series resistance, charge-transfer coefficient, and diffusion coefficient). Additionally, Levenberg-Marquardt optimizer, applied in [27], further refined membrane conductivity together with anode and cathode exchange currents. Although these deterministic optimizers can produce accurate results, their performance often hinges on good initial guesses and may degrade on large, highly nonlinear cost surfaces [28].

On the other hand, metaheuristic algorithms have shown excellent performance in tackling high nonlinear, complex, and operation-dependent optimization problems [29]. By adjusting their control parameters, they can offer optimal solutions with low computational burden [30]. Thus, they are widely utilized in various electrical engineering problems, such as optimal frequency regulation of microgrids [31], photovoltaic (PV) [32], battery [33], optimal distributed generators placement [34], and fuel cells parameter estimation [35, 36].

This encourages the authors in [37] to apply the particle swarm optimizer (PSO) to estimate three parameters of the PEMEZ model. Furthermore, bald eagle search optimizer (BESO) is employed in [38] to optimally identify six parameters adopting the least quadratic deviation as the objective function (F_{obj}). Moreover, the same authors in [39] have utilized honey badger algorithm (HBA) to determine the optimal values of seven parameters under two different operating conditions. For the same purpose, a modified version of HBA (MHBA), along with grey wolf optimizer (GWO), and PSO are introduced in [40] to optimally allocate eight parameters. The authors also investigated the impact

of varying the temperature and pressure on the simulated V-J, hydrogen flow rate, and voltage efficiency curves. However, further commercial testcases are required to validate the proposed methodology results.

According to the above-mentioned short survey, metaheuristic algorithms have become dominant in PEMEZ parameter estimation research due to their robustness and effectiveness in handling complex nonlinear problems. Indeed, the no-free lunch theory explains the inspiration of applying several algorithms for the same optimization problem. It states that no single algorithm can handle all optimization problems with the same effectiveness and robustness [41]. This highlights that there is always room for further improvement in metaheuristic optimizers concerning structural complexity, ability to explore broader search spaces, convergence trend, and computational efficiency.

1.3. Article contributions and structure

Based on the aforementioned illustrations, the literature still lacks a single integrated work that can (i) utilize such optimizers to fully define the electrochemical model, considering all empirical parameters, (ii) address practical physical variables of PEMEZs, such as partial pressures of hydrogen and oxygen, (iii) verify the efficacy of the optimization methodology under varying the PEMEZ operating conditions, and (iv) validate the practicability of the optimizer-based electrochemical model over different commercial testcases. This motivates the authors to propose a novel optimization methodology based on weighted mean of vectors algorithm (WMVA) [42] to address all the previously mentioned gaps. In fact, it's not the first time to apply WMVA in parameter estimation optimization problems. Specifically, WMVA has been implemented to optimally extract the seven ungiven parameters of PEM fuel cells [43]. Moreover, the authors in [44] applied WMVA to estimate the equivalent circuit model parameters of Li-Ion batteries. WMVA also was adopted for maximum power point tracking of PV systems as in [45].

To summarize, the main contributions of this work are as follows: (i) Proposing a quantitatively validated modelling strategy for PEMEZs utilizing the WMVA to address the nonlinear, multimodal, and interdependent nature of parameter estimation, (ii) Optimizing key electrochemical parameters that significantly enhance voltage prediction accuracy, potentially improving system reliability, (iii) Validating the robustness and accuracy of the proposed methodology across three commercial PEMEZ testcases from different manufacturers under varying operating conditions, (iv) Analysing the effects of temperature and hydrogen pressure on the electrical and physical steady-state performance of PEMEZs to highlight their impact on efficiency and longevity, (v) Demonstrating the WMVA's superior performance through a comprehensive statistical comparison with seven benchmark optimizers, and (vi) Conducting dynamic simulations to illustrate the dependence of hydrogen

production on temperature and supplied current, providing valuable insights for optimizing PEMEZ operation under diverse scenarios.

The reminder of this article is organized as follows: Section 2 offers a detailed mathematical formulation of PEMEZ electrochemical model. Section 3 introduces the inspiration and implementation procedure of the proposed WMVA. The assigned objective function along with its inequality constraints are mathematically expressed in Section 4. The numerical simulations for three commercial testcases are revealed in Section 5. Section 6 portraits a set of statistical analyses to evaluate the WMVA computational performance compared to other competitors. The impact of variable operating conditions on steady-state and dynamic response of PEMEZ is addressed in Section 7. Section 8 provides the conclusion and discusses future perspectives.

2. Electrochemical mathematical modelling

As concluded from the above survey, the electrochemical model is the most competent mathematical tool to simulate the polarization characteristics (V-J) of PEMEZs [37]. Particularly, it assumes that the PEMEZ electrical response is represented by a voltage source alongside three adjacent overpotential losses, as shown in Fig. 1(a) [38]. Physically, the voltage source represents the minimum electrical potential required to initiate the water-electrolysis reaction. In Fig. 1(b), the resulting polarization curve is annotated with shaded bands and callouts delineating the three dominant loss regimes [40]. Specifically, activation polarization is observed as a steep voltage rise at low current densities, while ohmic polarization appears as a nearly linear voltage increase at intermediate current densities. Finally, concentration polarization manifests as a sharp voltage rise at high current densities.

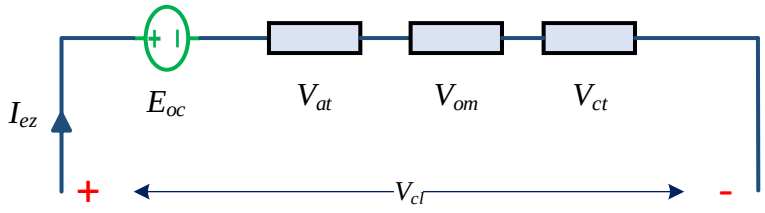

(a) Electrical equivalent circuit

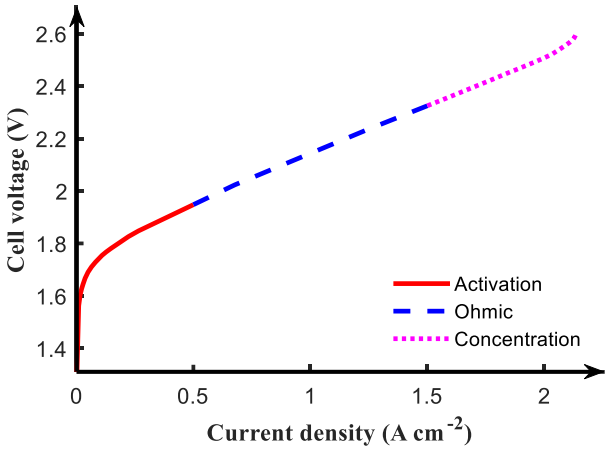

(b) Practical polarization curve

Fig. 1. Electrochemical model characteristics

Technically, a group of PEMEZ cells are gathered serially to augment hydrogen production rate, forming a PEMEZ stack. Hence, the stack output voltage $V_{st/z}$ in (V) is represented by (1).

$$V_{st/z} = N_z \times V_{cl/z} \tag{1}$$

where, $V_{cl/z}$ denotes the output voltage of a single PEMEZ cell which is expressed by (2) [38-40]. The number of series cells is symbolized by N_z.

$$V_{cl/z} = E_{oc} + V_{at} + V_{om} + V_{ct} \tag{2}$$

where, E_{oc} refers to the ideal lowest applied voltage needed to start the electrolysis in (V), calculated using Nernst formula, as shown in (3). The activation, ohmic, and concentration overpotentials are represented by V_{at}, V_{om}, and V_{ct} in (V), respectively.

$$E_{oc} = \frac{\Delta G}{2F} + \left[\frac{R \times T_z}{2F} \times ln\left(\frac{P_{Hy}\sqrt{P_{Ox}}}{P_{Wt}}\right)\right] \tag{3}$$

where, $R = 8.314 \times 10^{-3}$ kJ/mol. K is the universal gas constant and $F = 96.485$ kC/mol is the Faraday constant. The change in Gibbs-free-energy is denoted by ΔG in (kJ/mol). T_z is the PEMEZ operating temperature in (K). P_{Wt} represents the water pressure in (atm) and is calculated by (4). P_{Hy} and P_{Ox}, determined by (5) and (6), are the hydrogen and oxygen partial pressures in (atm), respectively.

$$P_{Wt} = 6.1078 \times 10^{-3} exp\left[17.2694\left(\frac{T_z - 273.15}{T_z - 34.85}\right)\right] \tag{4}$$

$$P_{Hy} = P_{ca} - P_{Wt} \tag{5}$$

$$P_{ox} = P_{an} - P_{Wt} \tag{6}$$

where, P_{an} and P_{ca} are the anode and cathode pressures in (atm), respectively.

In fact, the inclusion of P_{Hy} and P_{ox} in the electrochemical model is critical due to their direct influence on the thermodynamics and kinetics of the electrolysis reactions. Chemically, the equilibrium potentials explicitly depend on the partial pressures. Hence, accurately modelling these pressures ensures realistic simulation of cell voltage and efficiency, closely representing practical PEMEZ operation. Ignoring these partial pressures, as commonly done in previous literature, can significantly deviate the predicted performance from actual experimental observations, thus undermining the model's validity and reliability.

Specifically, V_{at} denotes the startup slowness of the chemical reaction, which dominates the initial loading phase of PEMEZ. Thus, V_{at} is mathematically given by (7).

$$V_{act} = \frac{R \times T_z}{2F \times \zeta_{an}} \sinh^{-1}\left(\frac{J_z}{2J_{an}^{ex}}\right) + \frac{R \times T_z}{2F \times \zeta_{ca}} \sinh^{-1}\left(\frac{J_z}{2J_{ca}^{ex}}\right) \tag{7}$$

where, J_z is the PEMEZ operating current density in $(\mathrm{A.\,cm^{-2}})$. The exchange current densities of the anode and cathode are represented by J_{an}^{ex} and J_{an}^{ex} in $(\mathrm{A.\,cm^{-2}})$, respectively. ζ_{an} and ζ_{ca} are the charge transfer coefficients for anode and cathode, respectively.

On the other side, the ohmic losses V_{om} due to the overall resistance experienced by PEMEZ is given by (8).

$$V_{om} = J_z \cdot (R_m + R_{el}) \tag{8}$$

where, R_m refers to the PEM resistance in $(\Omega.\,\mathrm{cm^{-2}})$ which is described by (9). The resistance from all other electrical paths, including current collectors, electrode materials, and connections is denoted by R_{el} in $(\Omega.\,\mathrm{cm^{-2}})$.

$$R_m = \frac{t_{mb}}{\sigma_{mb} \times A_{mb}} \tag{9}$$

where, the thickness and the active membrane area of the PEM are symbolized by t_{mb} in (cm) and A_{mb} in $(\mathrm{cm^2})$, respectively. The PEM conductivity, given by (10), is denoted by σ_{mb} in $\left(\Omega/\mathrm{cm^{2^{-1}}}\right)$.

$$\sigma_{mb} = (0.005139\beta - 0.00326) \cdot \exp\left[1268\left(\frac{1}{303} - \frac{1}{T_z}\right)\right] \tag{10}$$

Finally, at higher load conditions, increased water content in the membrane β leads to the emergence of concentration losses V_{ct}. Such losses can be determined by (11).

$$V_{ct} = \frac{R \times T_z}{2F} \times ln\left(\frac{J_{lim}}{J_{lim} - J_z}\right) \tag{11}$$

where, J_{lim} is the limited current density of PEMEZ in $(\mathrm{A.\,cm^{-2}})$.

The total efficiency of a PEMEZ is composed of three key terms: Faraday efficiency, thermodynamic efficiency, and voltage efficiency. However, since this paper focuses specifically on the electrical behaviour of the PEMEZ, only the voltage efficiency η_v is considered, as expressed in (12).

$$\eta_v = \frac{E_{oc}}{V_{cl/z}} \tag{12}$$

In addition, the theoretical hydrogen flow rate M_{Hy} in $(\mathrm{mol/h})$ is described in (13) [20].

$$M_{Hy,th} = \frac{N_z \times T_z \times R \times J_z \times A_{mb}}{2F \times P_{Hy}} \tag{13}$$

However, the actual hydrogen flow rate $M_{Hy,ss}$ in $(\mathrm{mol/h})$ is determined by (14) [46].

$$M_{Hy,ss} = M_{Hy,th} \times \eta_{Hy} \tag{14}$$

where, η_{Hy} is the hydrogen production efficiency which is empirically formulated in (15) [46].

$$\eta_{Hy} = c_1 \times exp\left(\frac{c_2 + c_3 \times T_z}{J_z}\right) \tag{15}$$

where, c_1, c_2, and c_3 are fitting parameters in (%), $(\mathrm{A/cm^2})$, and $(\mathrm{A/(cm^2 °C)})$, respectively.

Now, it's evident that ΔG, ζ_{an}, ζ_{ca}, J_{an}^{ex}, J_{ca}^{ex}, J_{lim}, β, and R_{el} are the unknown parameters in the electrochemical model that must be accurately estimated to ensure the model's outcomes align with experimental records.

3. Weighted mean of vectors algorithm (WMVA)

Principally, the WMVA is population-based optimizer inspired by the concept of combining vectors in a weighted manner to achieve an optimal solution in multi-dimensional search spaces [42]. Such vectors represent the possible solutions available within the search space. Accordingly, WMVA seeks the best vector position (solution) during a specified number of iterations IT_{mx} [43]. Specifically, since it's a population-based algorithm, WMVA operates with a population consisting of N_{pp} vectors within a search space defined by N_d dimensions $\left(x_{l,j}^{it} = \{x_{l,1}^{it}, x_{l,2}^{it}, \dots, x_{l,N_d}^{it}\}, l = 1,2, \dots N_{pp}\right)$. The initialization phase is governed by two control coefficients, namely weighted mean coefficient δ and scaling coefficient α, which are iteratively adjusted as shown in (16)-(17), respectively [44].

$$\delta = \left[2exp\left(\frac{-4it}{IT_{mx}}\right)\right] \times (2 \times rnd - 1) \tag{16}$$

$$\alpha = \left[2exp\left(\frac{-4it}{IT_{mx}}\right)\right] \times (2 \times rnd - 1) \tag{17}$$

where, it is the current iteration and rnd is a random generated number between 0 and 1.

Practically, WMVA comprises three key subprocesses for updating the positions of vectors in each iteration: updating rule, vector combining, and local search [45].

3.1. Updating rule phase

At the outset of WMVA, population diversity is improved using the mean operator M_o, as defined in (18)-(20). This operator is based on calculating the weighted average of a group of vectors chosen through differential selection [42].

$$M_o = r_1 \times WM1_l^{it} + (1 - r) \times WM2_l^{it} \tag{18}$$

$$WM1_l^{it} = \delta \times \frac{\omega_1(x_{a_1} - x_{a_2}) + \omega_2(x_{a_1} - x_{a_3}) + \omega_3(x_{a_2} - x_{a_3})}{\omega_1 + \omega_2 + \omega_3 + \varepsilon} + \varepsilon \times rnd \tag{19}$$

$$WM2_l^{it} = \alpha \times \frac{\omega_1(x_{bt} - x_{br}) + \omega_2(x_{bt} - x_{wt}) + \omega_3(x_{br} - x_{wt})}{\omega_1 + \omega_2 + \omega_3 + \varepsilon} + \varepsilon \times rnd \tag{20}$$

where, ω_1, ω_2, and ω_3 denote wavelet functions as outlined in [42, 44]. r_1 and ε represent a random value drawn from the interval [0, 0.5] and a small constant to prevent computational errors like division by zero, respectively. The integers a_1, a_2, and a_3 are distinct and randomly selected within the range [1, N_v]. Furthermore, x_{wt}, x_{br}, and x_{bt} refer to the worst, better, and best solutions among the population, respectively.

At this phase, the WMVA integrates a convergence operator C_o , as defined in (21), to further strengthen its search efficiency and improve solution refinement.

$$C_o = rndn \times \frac{x_{bt} - x_{a_1}}{f(x_{bt}) - f(x_{a_1}) + \varepsilon} \tag{21}$$

where, $rndn$ denotes normal distribution-based value. The fitness value of the vector x is symbolized by $f(x)$.

Once the preceding operators have been computed, the updated vector y_l^{it} can be determined by (22).

$$y_l^{it} = x_l^{it} + \left[2exp\left(\frac{-4it}{IT_{mx}}\right)\right] \times M_o + C_o \tag{22}$$

Lastly, the WMVA implements the exploration phase which comprises two updating scenarios based on the value of r. Both scenarios are function of x_l^{it}, $x_{a_1}^{it}$, x_{bt}, and x_{br}, as described in (23)-(24).

$$r_1 < 0.5 \xrightarrow{yields} \begin{cases} y1_l^{it} = x_l^{it} + \left[2exp\left(\frac{-4it}{IT_{mx}}\right)\right] \times M_o + rndn \times \frac{x_{bt} - x_{a_1}^{it}}{f(x_{bt}) - f(x_{a_1}^{it}) + 1} \\ y2_l^{it} = x_{bt} + \left[2exp\left(\frac{-4it}{IT_{mx}}\right)\right] \times M_o + rndn \times \frac{x_{a_1}^{it} - x_{a_2}^{it}}{f(x_{a_1}^{it}) - f(x_{a_2}^{it}) + 1} \end{cases} \tag{23}$$

$$r_1 \geq 0.5 \xrightarrow{yields} \begin{cases} y1_l^{it} = x_l^{it} + \left[2exp\left(\frac{-4it}{IT_{mx}}\right)\right] \times M_o + rndn \times \frac{x_{a_2}^{it} - x_{a_3}^{it}}{f(x_{a_2}^{it}) - f(x_{a_3}^{it}) + 1} \\ y2_l^{it} = x_{bt} + \left[2exp\left(\frac{-4it}{IT_{mx}}\right)\right] \times M_o + rndn \times \frac{x_{a_1}^{it} - x_{a_2}^{it}}{f(x_{a_1}^{it}) - f(x_{a_2}^{it}) + 1} \end{cases} \tag{24}$$

where, the new generated vectors at it^{th} iteration are denoted by $y1_l^{it}$ and $y2_l^{it}$.

3.2. Vector combining phase

Mainly, this phase is included in the algorithm to refine the local search process and expand the diversity within the population. Mathematically, $y1_l^{it}$ and $y2_l^{it}$ are combined with x_l^{it} to from a new vector z_l^{it} according to two random generated values $rand1$ and $rand2$, as outlined in (25)-(27) [43].

$$z_l^{it} = y1_l^{it} + (0.05 \times rndn) \times \left| y1_l^{it} - y2_l^{it} \right|, \qquad rnd1 < 0.5 \,\&\, rnd2 < 0.5 \tag{25}$$

$$z_l^{it} = y2_l^{it} + (0.05 \times rndn) \times \left| y1_l^{it} - y2_l^{it} \right|, \qquad rnd1 < 0.5 \,\&\, rnd2 \geq 0.5 \tag{26}$$

$$z_l^{it} = x_l^{it}, \qquad rnd1 \geq 0.5 \tag{27}$$

3.3. Local search phase

Finally, the WMVA enhances its exploitation phase by including a local search step designed to accelerate convergence toward the optimal solution while avoiding local optima. This is done by applying the mean operator along with the global position, and then generating a new vector using a revised updating rule, as shown in (28)-(31) [44].

$$z_l^{it} = \begin{cases} x_{bt} + rndn \times \left[M_o + rndn \times \left(x_{bt}^{it} - x_{a_1}^{it} \right) \right], & rnd < 0.5 \\ x_{rnd} + rndn \times \left[M_o + rndn \times (\rho_1 \times x_{bt} - \rho_2 \times x_{rnd}) \right], & rnd \geq 0.5 \end{cases} \tag{28}$$

$$x_{rnd} = \frac{r_2 \times (x_1 + x_2 + x_3)}{3} + (1 - r_2) \times [r_2 \times x_{br} + (1 - r_2) \times x_{bt}] \tag{29}$$

$$\rho_1 = \begin{cases} 2 \times rnd, & rnd > 0.5 \\ 1, & rnd \leq 0.5 \end{cases} \tag{30}$$

$$\rho_2 = \begin{cases} rnd, & rnd < 0.5 \\ 1, & rnd \geq 0.5 \end{cases} \tag{31}$$

where, r_2 is a stochastic generated number from 0 to 1.

Lastly, Fig. 2 demonstrate the systematic procedure of implementing the WMVA.

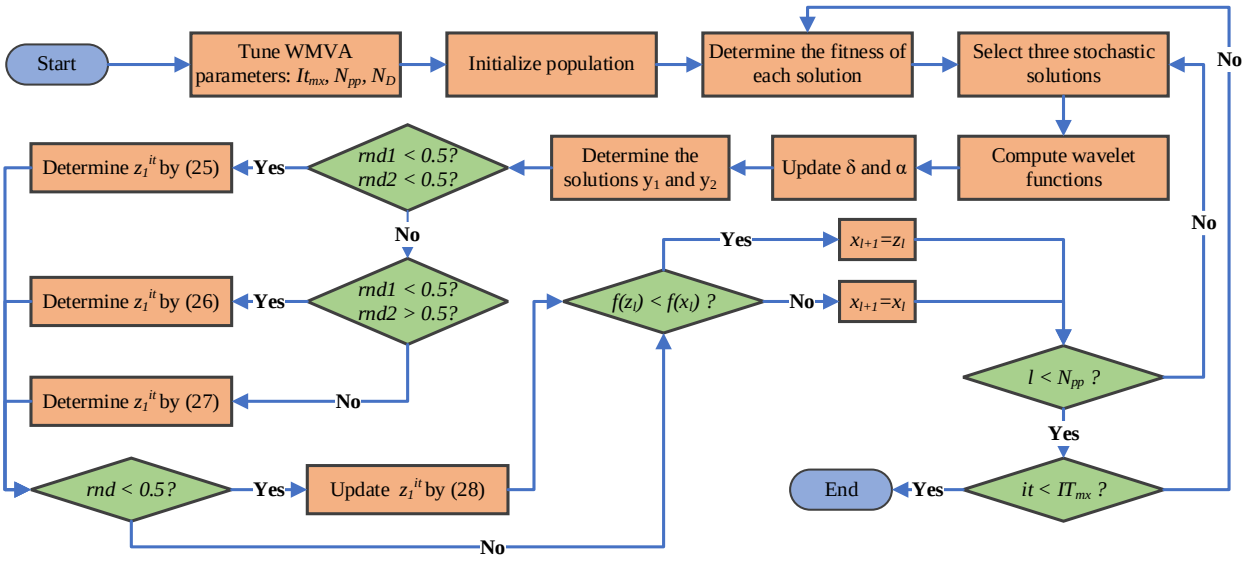

Fig. 2. Flowchart of WMVA

Furthermore, The Big-O notation is employed to evaluate the computational complexity of the WMVA by analysing its runtime as a function of the input parameters, as described by (32) [42].

$$O(WMVA) = O\left(IT_{mx} \times \left(N_{pp} \times N_D\right)\right) = O\left(IT_{mx} N_{pp} N_D\right) \tag{32}$$

Thus, $O\left(IT_{mx} N_{pp} N_D\right)$ implies that the computational effort scales linearly with the number of iterations, the population size, and the dimensionality of the problem, respectively. It highlights how increasing any of these factors will proportionally affect the algorithm's runtime.

4. Optimization problem specification

In the parameter estimation process for the PEMEZ, the objective function (F_{obj}) plays a crucial role in guiding the optimization algorithm. Thus, minimizing the mean squared deviation (MSD) between the experimentally measured voltages $V_{st/z,ex}^{k}$ and the model-predicted voltages $V_{st/z,cp}^{k}$ is defined here as the F_{obj} for the WMVA, as shown in (33) [40]. Specifically, the MSD quantifies the discrepancy by averaging the squared differences across all data points, as described in (34). Hence, it provides a robust metric to evaluate the accuracy of the electrochemical model. By minimizing the MSD, the WMVA ensures that the estimated parameters align the model's predictions closely with experimental observations. Such methodology enhances the model reliability and precision under various operating conditions.

$$F_{obj}(WMVA) = Minimize(MSD) \tag{33}$$

$$MSD = \frac{1}{N_{ex}} \sum_{k=1}^{N_{ex}} \left(V_{st/z,ex}^{k} - V_{st/z,cp}^{k} \right)^2 \quad (34)$$

where, N_{ex} denotes the number of the measured voltage values of PEMEZ.

To ensure realistic and physically meaningful solutions, lower and upper limits are imposed on the eight unknown parameters of the electrochemical model, as publicized in Table 1 [38-40]. These bounds constrain the search space, preventing the WMVA from exploring non-viable parameter values and enhancing the efficiency of the optimization process.

Table 1. Feasible limits of the electrochemical model unknown parameters

Parameter	$\Delta G, (\mathrm{kJ.mol^{-1}})$	ζ_{an}	ζ_{ca}	$J_{an}^{ex}, (\mathrm{A.cm^{-2}})$	$J_{ca}^{ex}, (\mathrm{A.cm^{-2}})$	$J_{lm}, (\mathrm{A.cm^{-2}})$	β	$R_{el}, (\Omega)$
Lower limit	0	0.1	0.25	10e-08	0.18	$\max\left(\sum_{k=1}^{N_{ex}} I_{z,ex}(k)\right)$	10	0.1
Higher limit	245	0.9	0.64	10e-06	0.39	3	24	0.8

5. Optimization numerical and graphical results

Herein, the WMVA along with seven well-known optimizers, namely artificial ecosystem optimizer (AEO) [47], educational competition optimizer (ECO) [48], equilibrium optimization algorithm (EOA) [47], gradient-based optimizer (GBO) [49], puma optimization algorithm (POA) [50], red-billed blue magpie optimizer (RBMO) [51] and secretary bird optimizer (SBO) [52] are executed for optimal identification of the PEMEZ electrochemical model. Furthermore, the results of these optimizers are compared to benchmark algorithms reported in the literature, like GWO, PSO, HBA, MHBA, and BESO. Three commercial testcases from different PEMEZ manufacturers (i.e. Giner Electrochemical Systems and HGenerators^{TM}) are carefully addressed for practical evaluation of the optimizers' efficacy in refining the electrochemical model outputs. Table 2 elucidates the technical characteristics of these testcases [13, 20, 38-40, 46, 53, 54]. It is worth noting that all algorithms share the same final selected values for IT_{mx} and N_{pp}, set to 300 and 30, respectively. Moreover, due to the significant randomness associated with such metaheuristic optimizers, the best results are determined by performing 20 independent runs for each testcase. In addition, for ensuring unbiased comparison, all simulations are conducted via MATLAB R2023b on a Dell laptop with an Intel® Core i7-13650HX processor running at 2.6 GHz and 16 GB of RAM.

Table 2. Technical specs of the studied testcases

Technical specs / Testcases		N_{cl}	$A_{mb}(\mathrm{cm^2})$	$t_{mb}, (\mathrm{cm})$	$T_z, (\mathrm{K})$	$P_{an}, (\mathrm{bar})$	$P_{ca}, (\mathrm{bar})$
Testcase (1)	Scenario 1	1	160	0.05	353.15	0.9	1
	Scenario 2				323.15	0.5	30
Testcase (2)	Scenario 1	12	160	0.0178	313.15	1	10
	Scenario 2				328.15	7	70
Testcase (3)		12	50	0.0178	323.15	1	1

Specifically, the next subsections discuss the numerical and graphical results of the proposed optimization methodology for each testcase individually.

5.1. Testcase (1)

This testcase is widely utilized in the context of PEMEZ parameter estimation due to its extensive availability of V-J datasets for two distinct operating scenarios [20]. The first scenario consists of 57 J-V data points measured at 80°C and a hydrogen pressure of 1 bar, while the second scenario provides 37 J-V data points recorded at 50°C and a hydrogen pressure of 30 bar (refer to Table 2) [13, 39]. In fact, it represents a commercial PEMEZ cell capable of operating at a maximum hydrogen pressure of 35 bar, with a temperature range of 50 °C to 80 °C, and producing hydrogen at a rate of 0.15 m^3/h [40]. Table 3 presents the numerical results of the proposed WMVA alongside those obtained from other executed and previously reported optimizers for both operating scenarios. As shown in Table 3, the WMVA achieves the lowest MSD values, recording 1.73366e-06 and 1.91934e-06 for the first and second scenarios, respectively.

Table 3. Estimated parameters for both scenarios of testcase (1)

Parameters / Algorithms	ΔG, ($\mathrm{kJ.mol^{-1}}$)	ζ_{an}	ζ_{ca}	J_{an}^{ex}, ($\mathrm{A.cm^{-2}}$)	J_{ca}^{ex}, ($\mathrm{A.cm^{-2}}$)	J_{lm}, ($\mathrm{A.cm^{-2}}$)	β	R_{el}, (Ω)	MSD, ($\mathrm{V^2}$)
Scenario (1)									
WMVA	**241.14570**	**0.36683**	**0.63999**	**9.9925e-06**	**0.33409**	**2.29899**	**23.8419**	**0.11553**	**1.73366e-06**
AEO	233.73854	0.36577	0.63870	4.0672e-06	0.34102	2.29863	21.7758	0.10134	1.73473e-06
ECO	235.57578	0.34234	0.63392	9.9075e-06	0.38596	2.32817	23.7630	0.11285	3.50363e-06
EOA	205.79741	0.36971	0.63845	1.0731e-07	0.38999	2.41111	21.1225	0.10001	2.08467e-06
GBO	236.47881	0.36623	0.63999	5.6584e-07	0.33880	2.29982	23.4294	0.11295	1.73381e-06
POA	238.93336	0.36228	0.63189	8.3868e-07	0.38999	2.31790	23.9933	0.11722	1.75616e-06
RBMO	228.91394	0.36995	0.62013	1.9973e-06	0.31615	2.29135	22.3990	0.10514	1.74743e-06
SBOA	240.90691	0.37000	0.63903	9.02634e-07	0.31383	2.29777	23.9977	0.11640	1.73964e-06
GWO[40]	222.23000	0.37300	0.57400	8.9300e-07	0.35600	2.30800	21.4300	0.19300	1.44000e-05
HBA[39]	229.96000	0.40700	0.50700	1.0000e-06	0.25600	2.22000	-	0.25400	6.84211e-06
MHBA[40]	222.72000	0.38500	0.64000	7.1500e-07	0.29700	2.14000	21.2200	0.14500	8.73000e-06
PSO[40]	222.34000	0.37500	0.63900	1.0500e-06	0.38700	2.30100	21.5900	0.14500	1.33000e-05
Scenario (2)									
WMVA	**244.99982**	**0.31576**	**0.63999**	**9.5196e-07**	**0.39000**	**1.84747**	**23.9999**	**0.17155**	**1.91934e-06**
AEO	244.74906	0.31608	0.59462	9.1484e-07	0.38998	1.82343	19.7169	0.12472	1.92037e-06
ECO	240.60139	0.32298	0.61559	4.4850e-07	0.33938	2.68603	17.5136	0.10000	2.34256e-06
EOA	244.81706	0.31805	0.57908	8.6367e-07	0.38283	1.84920	23.5830	0.16630	1.93925e-06
GBO	244.99998	0.31577	0.63855	9.5177e-07	0.38999	1.84631	23.9999	0.17149	1.91936e-06
POA	243.10570	0.31643	0.57180	7.4650e-07	0.36461	1.75717	18.6041	0.10672	1.93034e-06
RBMO	233.77982	0.31589	0.63999	2.5333e-07	0.38999	1.85190	23.6826	0.16890	1.91942e-06
SBOA	244.85521	0.31674	0.60630	9.0750e-07	0.37395	1.83207	23.6189	0.16658	1.92552e-06
GWO[40]	233.13000	0.32310	0.63990	1.9700e-07	0.30360	2.29000	20.6600	0.46900	1.12000e-05
HBA[39]	235.00000	0.31100	0.64000	3.6700e-07	0.39000	1.70000	-	0.36800	7.42105e-06
MHBA[40]	233.32000	0.31610	0.64000	2.5800e-07	0.38900	1.40000	20.6200	0.74000	8.75000e-06
PSO[40]	235.31000	0.31650	0.49000	3.0700e-07	0.39100	1.73000	21.2600	0.71900	9.78000e-06

To evaluate how the WMVA-optimized parameter values align the electrochemical model's calculated voltages with the experimental measurements, Figs. 3(a)-(b) and Figs. 4(a)-(b) illustrate the V-J and P-J curves for both scenarios, respectively. Figs. 3(a)-(b) and Figs. 4(a)-(b) clearly demonstrate that the calculated voltages closely match the experimentally measured values which underscores the effectiveness of the proposed WMVA-based electrochemical model.

On the other hand, Figs. 3(c)-(d) and Figs. 4(c)-(d) depict the variation in individual polarization losses and the voltage efficiency of the PEMEZ with changes in the supplied current under both operating conditions, respectively. As the current increases, activation and ohmic losses typically rise due to higher reaction rates and resistive effects. On the other side, concentration losses become more prominent at higher current densities. These losses collectively impact the overall voltage efficiency, which tends to decrease as the current grows since it reflects the increasing energy demand to sustain electrolysis under such conditions.

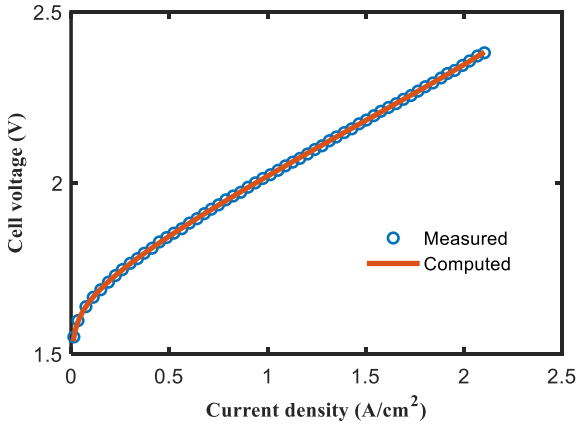

(a) V-J curve

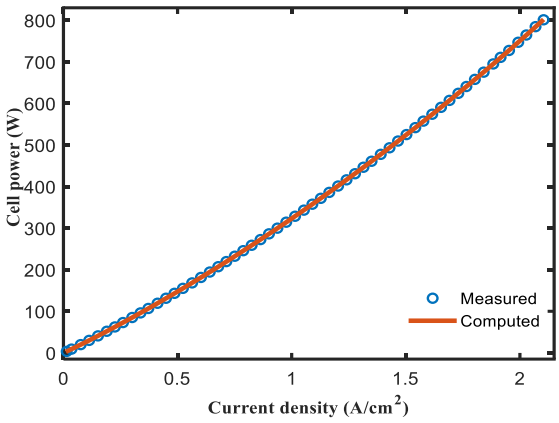

(b) P-J curve

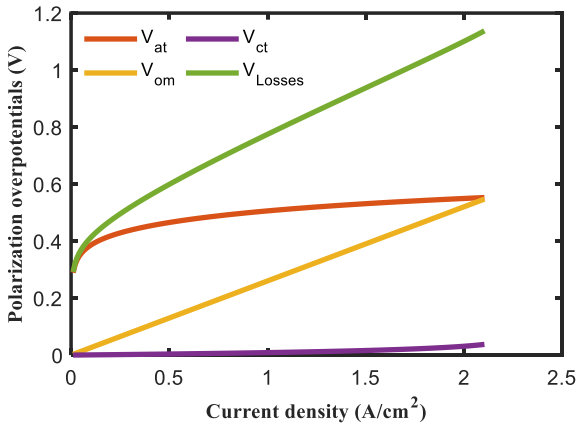

(c) Losses curve

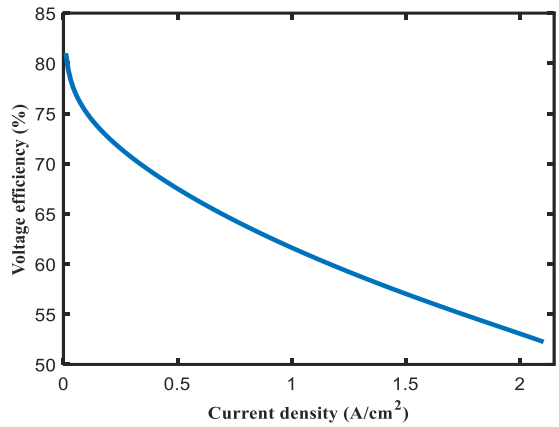

(d) Voltage efficiency curve

Fig. 3. Polarization characteristics for Testcase (1), Scenario (1)

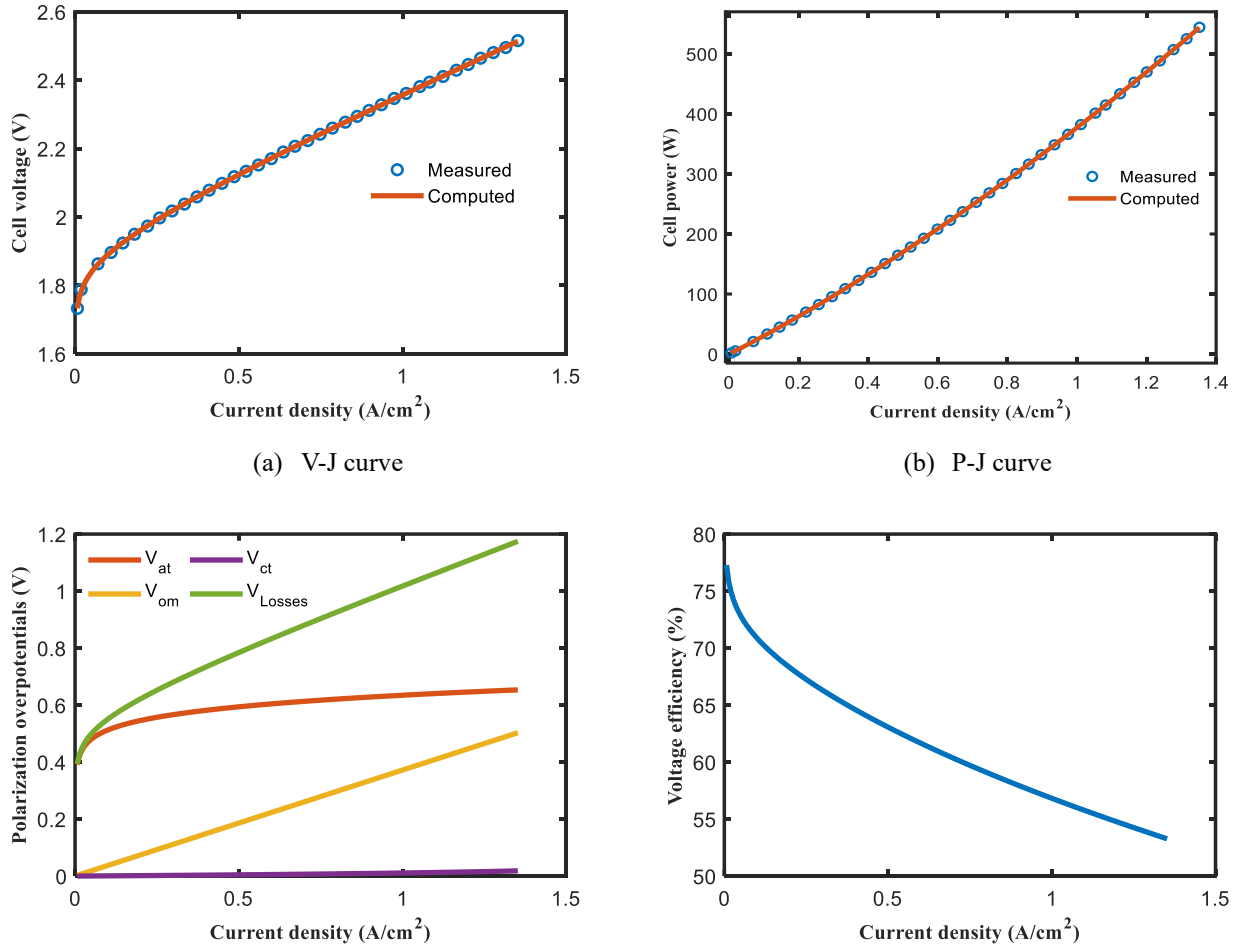

(a) V-J curve

(b) P-J curve

(c) Losses curve

(d) Voltage efficiency curve

Fig. 4. Polarization characteristics for Testcase (1), Scenario (2)

5.2. Testcase (2)

A high-pressure PEMEZ stack is presented in this study which is manufactured by Giner Inc. (Massachusetts, USA) [53, 54]. Specifically, the stack can produce 1.1 Nm³ of hydrogen per hour when operating at its maximum power (5.6 kW) [38]. Once again, two V-J datasets are reported in the literature, corresponding to different operating scenarios [40]. Scenario (1) includes 36 V-J points measured at an operating temperature of 40°C and a hydrogen pressure of 10 bar. Meanwhile, Scenario (2) presents 29 V-J points recorded at an operating temperature of 55°C and a hydrogen pressure of 70 bar. Herein, the WMVA continues its superiority to extract the optimal values of the eight unknowns by attaining the minimum MSD among all employed and reported competitors for both scenarios, as announced in Table 4. Numerically, the proposed WMVA achieves MSD values of 1.09306e-05 and 6.18248e-05 for Scenario (1) and Scenario (2), respectively. Figs. 5(a)-(b) provide a visual representation of how the WMVA-based results improved the alignment of the computed voltages with

the measured values for both scenarios. Similarly, the corresponding power curves are depicted in Figs. 5(c)-(d), respectively.

Table 4. Estimated parameters for both scenarios of testcase (2)

Parameters / Algorithms	ΔG, ($\mathrm{kJ.mol^{-1}}$)	ζ_{an}	ζ_{ca}	J_{an}^{ex}, ($\mathrm{A.cm^{-2}}$)	J_{ca}^{ex}, ($\mathrm{A.cm^{-2}}$)	J_{lm}, ($\mathrm{A.cm^{-2}}$)	β	R_{el}, (Ω)	MSD, ($\mathrm{V^2}$)
Scenario (1)									
WMVA	**239.77276**	**0.75604**	**0.63999**	**1.2869e-06**	**0.38999**	**1.50703**	**14.9129**	**0.39451**	**1.09306e-05**
AEO	243.15060	0.75677	0.63951	3.4006e-06	0.38999	1.50874	20.4304	0.43148	1.09312e-05
ECO	244.99962	0.75595	0.47075	6.3955e-06	0.33745	1.50030	10.0000	0.31513	1.17416e-05
EOA	245.00000	0.75586	0.63910	5.8864e-06	0.38999	1.50716	17.0643	0.41181	1.09312e-05
GBO	242.25166	0.75601	0.63999	2.6445e-06	0.39000	1.50700	23.1789	0.44304	1.09306e-05
POA	245.00000	0.75678	0.64000	5.8297e-06	0.39000	1.50803	24.0000	0.44611	1.09310e-05
RBMO	243.28448	0.75438	0.62795	3.6512e-06	0.38678	1.50305	19.7200	0.42709	1.09483e-05
SBOA	245.00000	0.75436	0.63999	5.9915e-06	0.39000	1.50568	10.0002	0.32491	1.09313e-05
GWO[40]	227.28000	0.57600	0.48900	3.3900e-07	0.37900	1.75000	14.3100	0.23300	6.09000e-05
MHBA[40]	226.87000	0.57100	0.63900	3.3100e-07	0.38900	2.31000	13.9900	0.64900	5.96000e-05
PSO[40]	226.26000	0.70400	0.25600	1.9400e-08	0.34100	1.81000	14.7700	0.10000	6.20000e-05
Scenario (2)									
WMVA	**196.72648**	**0.36021**	**0.25000**	**2.7497e-06**	**0.26870**	**2.99999**	**14.0500**	**0.50143**	**6.18248e-05**
AEO	204.95331	0.36097	0.25000	7.1116e-06	0.26455	2.99997	17.8104	0.52667	6.18300e-05
ECO	180.36944	0.35607	0.25000	3.1909e-07	0.30984	2.54391	24.0000	0.55591	6.27554e-05
EOA	206.46811	0.35748	0.25086	9.2797e-07	0.28423	2.98590	23.9946	0.55289	6.18859e-05
GBO	196.72623	0.36022	0.25000	2.4344e-07	0.26864	2.99823	22.0222	0.54506	6.18249e-05
POA	201.59002	0.35968	0.25079	4.6770e-06	0.26912	2.99090	20.1915	0.53811	6.18338e-05
RBMO	198.78966	0.36012	0.25003	3.2046e-06	0.26865	2.99401	19.8784	0.53684	6.18253e-05
SBOA	207.01548	0.35994	0.25336	9.5313e-06	0.26128	2.30530	15.3714	0.50911	6.19053e-05
BESO[38]	233.10000[a]	0.45810	0.35310	9.3700e-07	0.38910	9.99000*	-	-	3.48620e-05
GWO[40]	222.30000	0.45560	0.28540	9.9900e-07	0.18000	2.31400	11.7600	0.79900	1.36000e-04
MHBA[40]	222.77000	0.46310	0.25020	9.7900e-06	0.22820	2.49000	11.6300	0.69800	6.44000e-05
PSO[40]	222.30000	0.45000	0.64000	1.0000e-06	0.18000	2.01000	11.0600	0.80000	1.27000e-04

*The value violates the practical boundaries, so it's unfeasible solution.

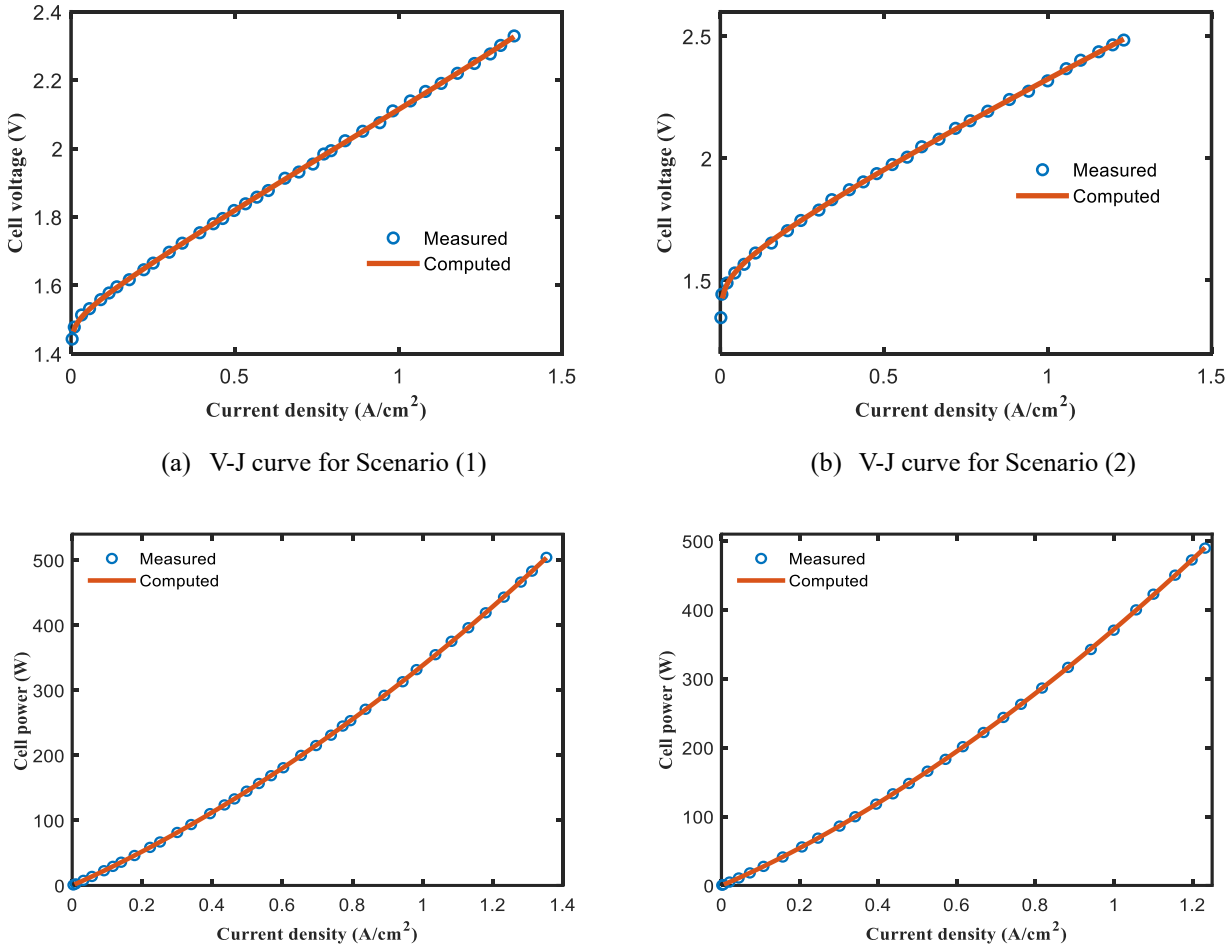

(a) V-J curve for Scenario (1)

(b) V-J curve for Scenario (2)

(c) P-J curve for Scenario (1)

(d) P-J curve for Scenario (2)

Fig. 5. Polarization curves for Testcase (2)

5.3. Testcase (3)

Herein, a 1 kW well-known commercial PEMEZ stack, called LM-2000 HGenerator^{TM}, is introduced to further validate the efficacy of the proposed WMVA. Particularly, a 50 V-J points, measured at an operating temperature of 50°C and a hydrogen pressure of 1 bar, are extracted from [46]. As expected, the WMVA continues to deliver the best MSD performance, achieving a value of 4.41586e-06, as captured in Table 5. Again, Figs. 6(a)-(b) describes the consistency between the experimentally recorded and model-based values for voltage and power, respectively.

Table 5. Estimated parameters for testcase (3)

Parameters / Algorithms	ΔG, (kJ. mol^{-1})	ζ_{an}	ζ_{ca}	J_{an}^{ex}, (A. cm^{-2})	J_{ca}^{ex}, (A. cm^{-2})	J_{lm}, (A. cm^{-2})	β	R_{el}, (Ω)	MSD, (V^2)
WMVA	**243.76977**	**0.25111**	**0.63999**	**4.6068e-06**	**0.38999**	**1.06934**	**19.9778**	**0.31272**	**4.41586e-06**
AEO	240.67898	0.25106	0.63994	3.4574e-06	0.38999	1.06931	20.9237	0.32555	4.41591e-06
ECO	243.55997	0.26988	0.64000	2.3355e-06	0.38999	3.00000	21.4662	0.36924	1.08888e-05
EOA	243.23045	0.24968	0.61926	4.6294e-06	0.38370	1.06488	23.1381	0.34896	4.45512e-06
GBO	243.20515	0.25127	0.63999	4.3440e-06	0.38954	1.06957	23.7398	0.35775	4.41683e-06
POA	244.99441	0.25165	0.64000	5.0520e-06	0.39000	1.06957	11.5505	0.10000	4.41854e-06
RBMO	243.41991	0.25513	0.63372	3.8083e-06	0.38978	1.07422	11.5023	0.10023	4.49763e-06
SBOA	244.10332	0.25053	0.63863	4.8614e-06	0.38904	1.06809	23.9975	0.35962	4.42023e-06

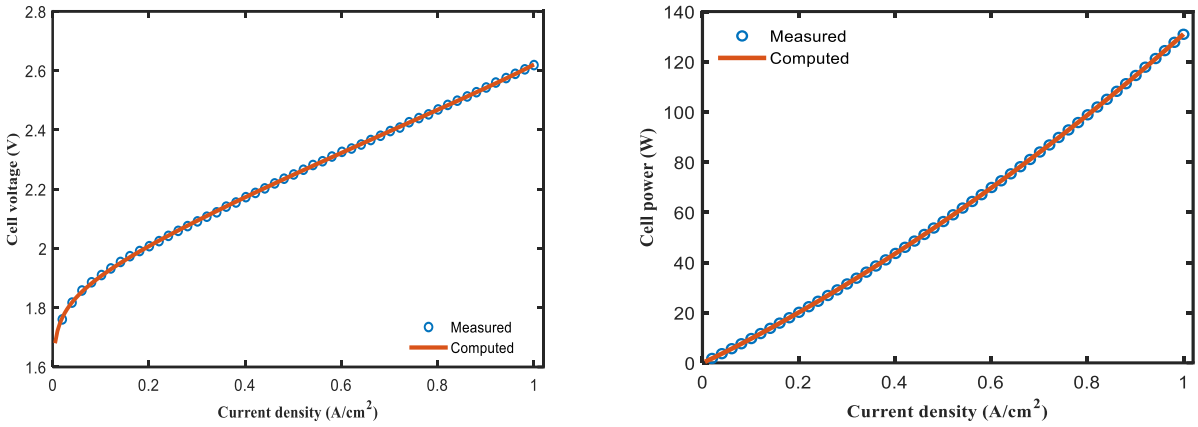

(a) V-J curve (b) P-J curve

Fig. 6. Polarization curves for Testcase (3)

6. Statistical and computational evaluation

After validating the superior performance of the WMVA over other executed optimizers in achieving the lowest MSD within the same number of iterations and independent runs, the focus shifts to evaluating the computational efficiency and randomness level of these algorithms.

6.1. Convergence trends

Firstly, the convergence patterns of all employed algorithms for the two scenarios of testcases (1) and (2) and testcase (3) are illustrated in Figs. 7(a)-(e), respectively. Through many of these curves, the WMVA demonstrates a faster decline in the F_{obj} value which indicates its ability to reach optimal solutions more efficiently. Additionally, its curve exhibits minimal oscillations which also reflects better stability and consistency during iterations. This highlights the robustness of the WMVA in maintaining a reliable convergence trend in terms of speed and precision, even in the face of complex optimization scenarios.

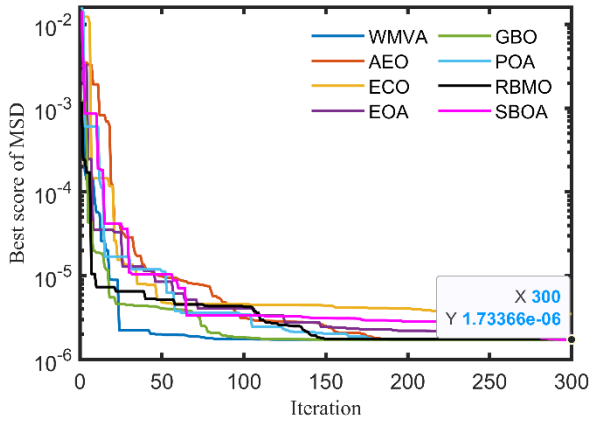

(a) Convergence of Testcase (1), Scenario (1)

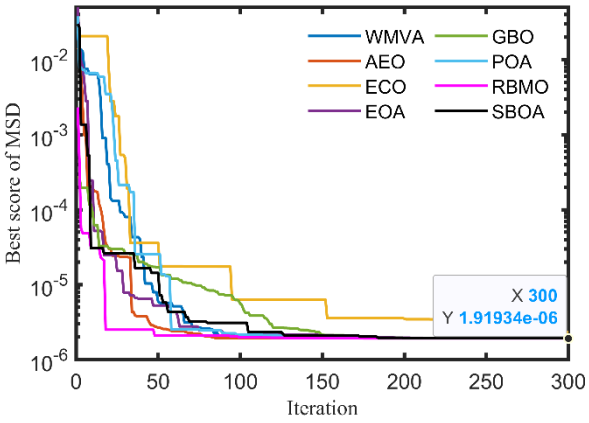

(b) Convergence of Testcase (1), Scenario (2)

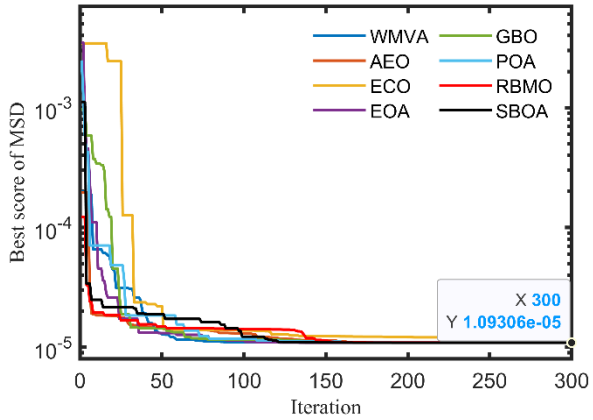

(c) Convergence of Testcase (2), Scenario (1)

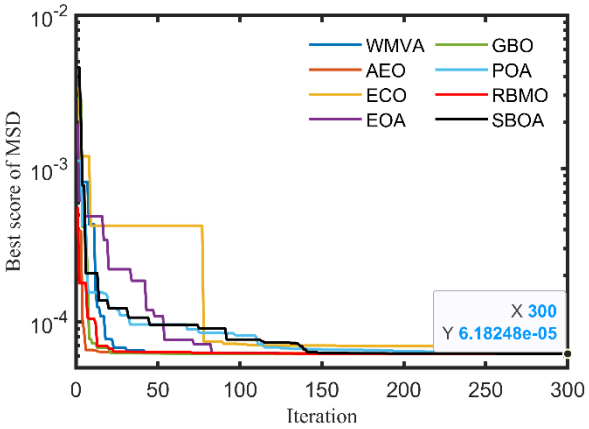

(d) Convergence of Testcase (2), Scenario (2)

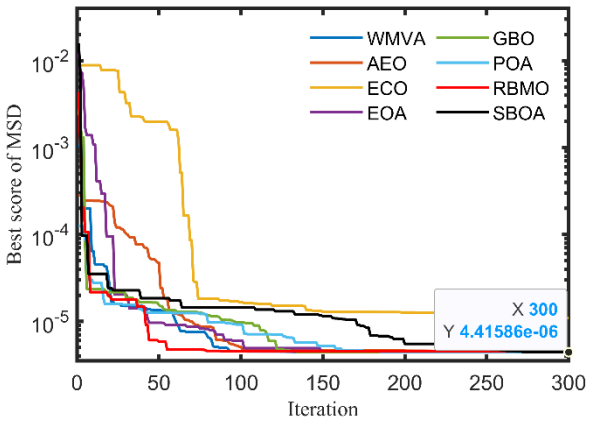

(e) Convergence of Testcase (3)

Fig. 7. Convergence curves for all testcases

6.2. Descriptive statistics

Moreover, Table 6 presents the outcomes of various statistical indices, including the standard deviation (StD) and variance, evaluated across 20 independent runs for all testcases. Particularly, StD measures the spread or dispersion of the results which highlights how much individual runs deviate from the

average performance. Similarly, the variance quantifies the extent of variability in the outcomes. Achieving the lowest values for these indices, as observed for the WMVA, signifies not only consistent performance across independent runs but also a high level of stability in delivering optimal solutions. This demonstrates the robustness of the WMVA in handling the parameter estimation problem with minimal randomness or unpredictability. Furthermore, the mean absolute percentage deviation (MAPD) is computed as per (35) and is summarized in Table 6 for each algorithm across all testcases. These metrics provide additional insights into the accuracy and precision of the algorithms.

$$\text{MAPD} = \frac{1}{N_{ex}} \sum_{k=1}^{N_{ex}} \frac{\left| V_{st/z,ex}^{k} - V_{st/z,cp}^{k} \right|}{V_{st/z,ex}^{k}} \times 100 \tag{35}$$

Unsurprisingly, the WMVA outperforms all other algorithms by achieving the lowest MAPD values across all testcases. This superior performance highlights the WMVA's remarkable accuracy in minimizing the deviation between the model-predicted and experimental values, as a percentage relative to the measured data.

6.3. Overall group comparison

A one-way ANOVA was applied to the final MSDs of all eight algorithms for each testcase to test whether their mean performances differ significantly. According to Table 6 (last column), all p-values fall below the 0.05 significance threshold, so the null hypothesis of equal mean MSDs is rejected in every case. Moreover, the boxplots in Fig. 8 reveal that WMVA consistently has both the lowest median MSD and the narrowest interquartile range across all three testcases. This indicates not only superior central accuracy but also tighter run-to-run consistency, thereby confirming WMVA’s overall advantage over the other optimizers.

6.4. Pairwise hypothesis tests against WMVA

To rigorously evaluate whether WMVA’s lower MSD truly outperforms each competing optimizer, two complementary paired tests across the 20 independent runs per testcase are employed. The Wilcoxon signed-rank test, a non-parametric method that makes no assumption of normality, examines whether the median of the paired MSD differences (WMVA minus other algorithm) differs from zero. The paired t-test, a parametric alternative, assesses whether the mean of those differences is significantly nonzero under the assumption of normality. In both cases we use a significance threshold of α=0.05. Table 6 (eighth and ninth columns) compiles the resulting p-values for each pairing and each of the three testcases.

Across all testcases, the Wilcoxon test consistently yields $p<0.05$ for every pairing, confirming that WMVA's median MSD is significantly lower than each competitor's. The paired t-test agrees in most cases, with significant p-values particularly against ECO, EOA, GBO, POA, and SBOA in nearly every scenario.

Only a handful of pairings, such as WMVA vs. AEO in Testcase (2), Scenario (1) and Testcase (3), or vs. RBMO in Testcase (3), fail the t-test despite a significant Wilcoxon result, suggesting some non-normality in those paired differences. Nonetheless, the uniform significance of the non-parametric tests underscores WMVA's robust and reproducible advantage in voltage-prediction accuracy.

6.5. Composite efficiency index (CEI)

To capture both accuracy and computational cost in a single metric, the composite efficiency index (CEI) for each algorithm i in each testcase is proposed. It combines the median MSD $\widetilde{MSD}_i$ and the median runtime $\tilde{T}_i$ of across the 20 independent runs, as describe by (36).

$$CEI_i = \frac{1}{2}(A_i + S_i) \tag{36}$$

where, A_i and S_i are the normalized $\widetilde{MSD}_i$ and $\tilde{T}_i$ to a [0,1] scale, which are computed by (37) and (38), respectively.

$$A_i = \frac{\widetilde{MSD}_{mx} - \widetilde{MSD}_i}{\widetilde{MSD}_{mx} - \widetilde{MSD}_{mn}} \tag{37}$$

$$S_i = \frac{\tilde{T}_{mx} - \tilde{T}_i}{\tilde{T}_{mx} - \tilde{T}_{mn}} \tag{38}$$

where, $\widetilde{MSD}_{mx}$, $\tilde{T}_{mx}$, $\widetilde{MSD}_{mn}$, $\tilde{T}_{mn}$ are the maximum and minimum median values of MSD and runtime for all algorithms per a certain testcase, respectively.

Here $A_i = 1$ denotes the best (lowest) median MSD and $S_i = 1$ denotes the best (fastest) median runtime. Accordingly, CEI_i is bounded by a [0,1] scale, with higher values indicating a better trade-off between accuracy and speed.

A closer look to Table 6 (seventh column), WMVA consistently achieves the highest CEI in every testcase, indicating that it provides the optimal trade-off between predictive accuracy and computational efficiency among all eight algorithms.

Table 6. Statistical analyses of WMVA and other competitors

Testcase	Scenario	Optimizer	Statistical indices						
			St.D	Variance	MAPD	CEI	Wilcoxon p-value vs WMVA	T-test p-value vs WMVA	ANOVA p-value
Testcase (1)	(1)	**WMVA**	**3.5887e-07**	**1.2879e-13**	**0.05433**	**0.995872**	-	-	1.89e-15
		AEO	9.1938e-07	8.4527e-13	0.05443	0.642948	0.005110	0.018100	
		ECO	1.0233e-05	1.0471e-10	0.06823	0.473440	0.000089	0.000327	
		EOA	1.6644e-06	2.7702e-12	0.06023	0.942648	0.000892	0.000429	
		GBO	1.2530e-06	1.5701e-12	0.05439	0.970896	0.003190	0.001360	
		POA	2.6001e-06	6.7607e-12	0.05476	0.941279	0.000338	0.009030	
		RBMO	1.2662e-06	1.6032e-12	0.05463	0.533316	0.001320	0.016100	
		SBOA	5.3747e-07	2.8888e-13	0.05476	0.489457	0.000120	0.000694	
	(2)	**WMVA**	**9.1266e-08**	**8.3295e-15**	**0.04905**	**1.000000**	-	-	0.03350
		AEO	9.3499e-08	8.7422e-15	0.04907	0.730663	0.002200	0.012200	
		ECO	4.0112e-05	1.6089e-09	0.05209	0.481902	0.000089	0.146000	
		EOA	1.9130e-06	3.6597e-12	0.04925	0.509222	0.000089	0.003600	
		GBO	9.6806e-07	9.3715e-13	0.04906	0.510211	0.000338	0.003390	
		POA	2.2823e-06	5.2087e-12	0.04906	0.488811	0.000517	0.048400	
		RBMO	9.3550e-06	8.7515e-11	0.04907	0.585442	0.000390	0.011700	
		SBOA	6.9887e-07	4.8841e-13	0.04909	0.531805	0.000103	0.000005	
Testcase (2)	(1)	**WMVA**	**4.1280e-08**	**1.7040e-15**	**0.14297**	**0.997549**	-	-	1.46e-05
		AEO	1.2517e-07	1.5668e-14	0.14303	0.903573	0.007190	0.410000	
		ECO	8.4396e-06	7.1227e-11	0.15058	0.493652	0.000103	0.029000	
		EOA	1.0071e-06	1.0142e-12	0.14304	0.982550	0.008970	0.459000	
		GBO	1.1230e-07	1.2611e-14	0.14301	0.828768	0.012400	0.846000	
		POA	1.2351e-06	1.5254e-12	0.14301	0.820035	0.000390	0.002030	
		RBMO	8.1023e-07	6.5648e-13	0.14317	0.521577	0.000780	0.000311	
		SBOA	5.7248e-07	3.2774e-13	0.14310	0.485319	0.005730	0.073400	
	(2)	**WMVA**	**2.7233e-07**	**7.4162e-14**	**0.28559**	**0.998404**	-	-	2.73e-35
		AEO	2.8679e-07	8.2252e-14	0.28589	0.650159	0.008970	0.006320	
		ECO	1.7362e-04	3.0145e-08	0.29274	0.497891	0.000089	0.000001	
		EOA	1.1593e-06	1.3439e-12	0.28794	0.990310	0.000140	0.000018	
		GBO	2.9780e-07	8.8688e-14	0.28559	0.991990	0.000390	0.000305	
		POA	9.8437e-07	9.6898e-13	0.28637	0.983514	0.001020	0.000419	
		RBMO	2.8127e-06	7.9113e-12	0.28585	0.528672	0.001160	0.002220	
		SBOA	5.2723e-07	2.7797e-13	0.28616	0.494901	0.000089	0.000017	
Testcase (3)		**WMVA**	**8.9664e-07**	**8.0396e-13**	**0.07835**	**0.991469**	-	-	0.00017
		AEO	1.3323e-06	1.7752e-12	0.07956	0.889168	0.047900	0.140000	
		ECO	1.6557e-04	2.7414e-08	0.11651	0.485750	0.000120	0.026000	
		EOA	5.8381e-06	3.4084e-11	0.08065	0.893297	0.005110	0.032300	
		GBO	2.5981e-06	6.7499e-12	0.07948	0.977850	0.000390	0.000274	
		POA	1.4169e-06	2.0077e-12	0.07953	0.962592	0.000120	0.282000	
		RBMO	1.3110e-05	1.7188e-10	0.07954	0.642661	0.000103	0.181000	
		SBOA	2.4801e-06	6.1507e-12	0.07979	0.469652	0.002820	0.002020	

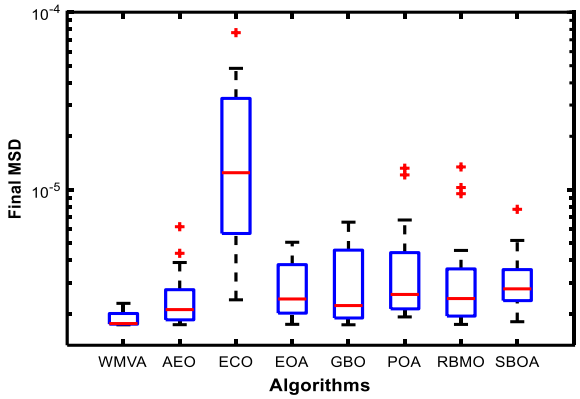

(a) Boxplots of Testcase (1), Scenario (1)

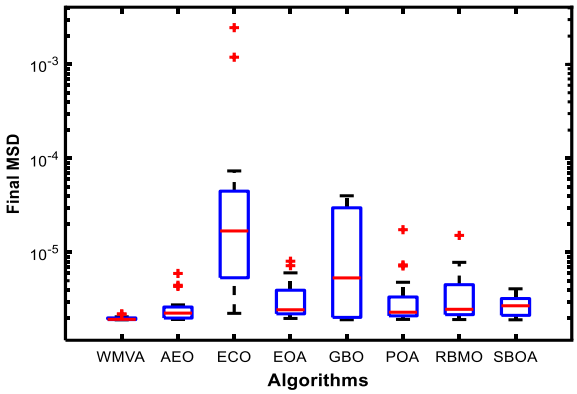

(b) Boxplots of Testcase (1), Scenario (2)

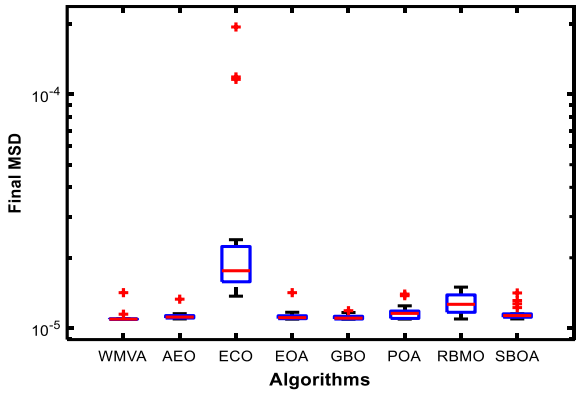

(c) Boxplots of Testcase (2), Scenario (1)

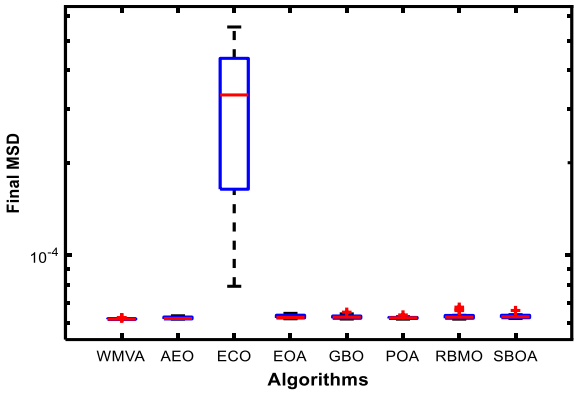

(d) Boxplots of Testcase (2), Scenario (2)

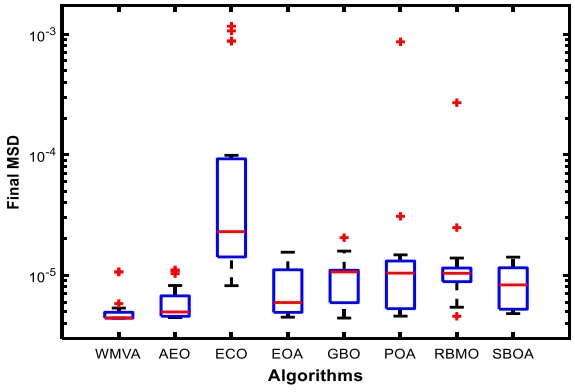

(e) Boxplots of Testcase (3)

Fig. 8. Boxplots of final MSD per run

7. Detailed assessment of PEMEZ performance

Based on the previously discussed validations, the WMVA-based electrochemical model has demonstrated remarkable adaptability and precision across various testcases and operating conditions. This signifies its effectiveness in accurately capturing the PEMEZ behaviour under diverse scenarios.

Thus, the aforementioned outcomes are utilized in this section for critical evaluation of PEMEZ to understand how changes in operating conditions influence its electrochemical performance. Additionally, the analysis focuses also on how variations in the supplied current and operating temperature dynamically affect hydrogen production.

7.1. Varying operating conditions

Herein, the effect of changing the operating temperature and hydrogen pressure on the PEMEZ steady-state performance is carefully studied for Testcase (1). Hence, Fig. 9 provides a detailed visualization of the PEMEZ's performance under varying operating temperatures of 50°C, 60°C, 70°C, and 80°C, with hydrogen and oxygen pressures fixed at 20 bar and 1 bar, respectively [40]. Specifically, Figs. 9(a)-(d) illustrate how the voltage profile, polarization losses, voltage efficiency, and hydrogen flow rate adjust in response to the temperature changes, respectively. This offers a comprehensive assessment of the electrochemical behaviour and operational efficiency under different thermal conditions.

According to Fig. 9(a), at low to moderate current densities, an increase in temperature causes the voltage to increase. This behaviour arises primarily due to the temperature's effect on activation losses, which are a significant component of the overall polarization losses in this range, as shown Fig. 9(b). Higher temperatures accelerate the electrochemical reaction rates at the electrodes, which increases the activation energy requirements. This results in a rise in the activation losses, which in turn leads to an increase in the overall cell voltage. However, at higher current densities, the effect of temperature often becomes inverse, as the reduction in ohmic resistance and other factors start to dominate the performance characteristics. On the other hand, concentration losses remain relatively unaffected unless mass transport limitations occur, as depicted in Fig. 9(b). Moreover, at low to moderate current densities, increasing temperature reduces the voltage efficiency due to higher activation losses, which raise the overall cell voltage, as described in Fig. 9(c). However, at higher current densities, the improved ionic conductivity at elevated temperatures reduces ohmic losses, which slightly lower cell voltage and enhance voltage efficiency. This highlights the complex relationship between temperature and current density in PEMEZ. Finally, the hydrogen flow rate increases with temperature, as higher thermal energy accelerates the electrolysis reaction, as illustrated in Fig. 9(d).

The same approach is employed for varying the hydrogen pressure (1 bar, 10 bar, 20 bar, and 35 bar), while maintaining the operating temperature at 80°C and oxygen pressure at 1 bar, as shown in Fig. 10. For the voltage profile, increasing hydrogen pressure typically raises the overall cell voltage due to increased internal resistance and pressure-induced changes in the electrochemical dynamics, as depicted in Fig. 10(a). However, polarization losses remain relatively stable across different pressures,

as revealed in Fig. 10(b). Additionally, Fig. 10(c) demonstrates that the voltage efficiency decreases because elevated pressure introduces additional resistance factors. Lastly, the hydrogen flow rate decreases with higher hydrogen pressure due to the interplay of the ideal gas law and Faraday's law.

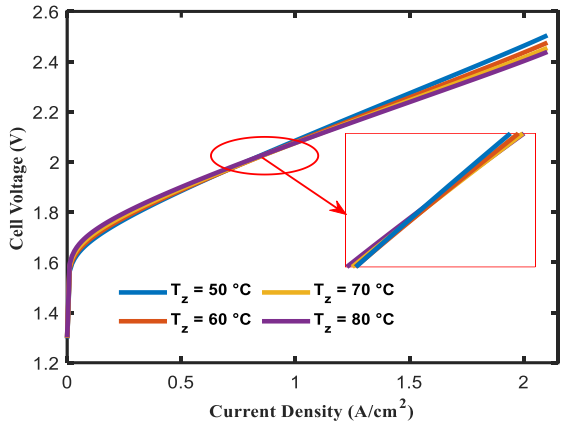

(a) V-J curves

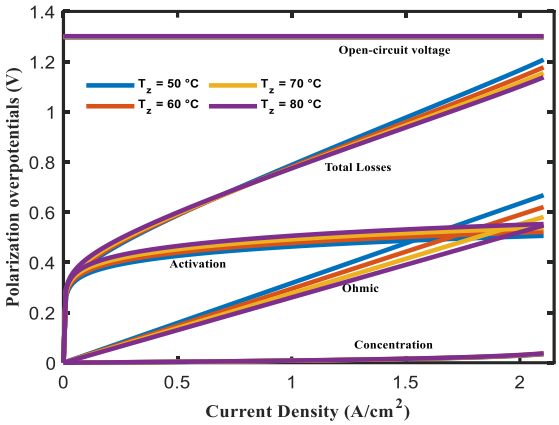

(b) Polarization losses curves

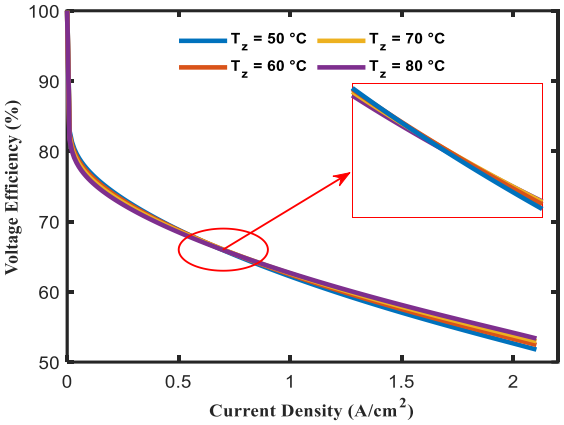

(c) Voltage efficiency curves

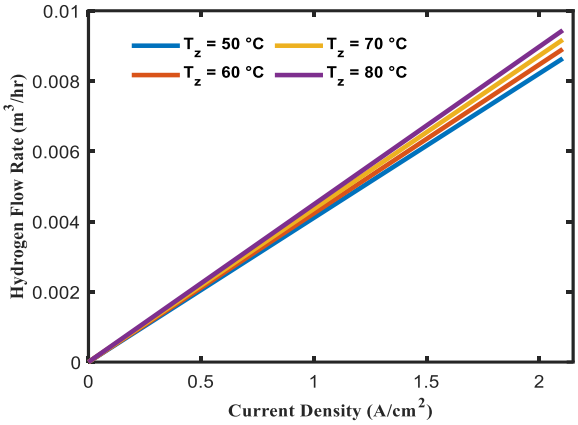

(d) Hydrogen flow rate curves

Fig. 9. Effects of varying temperature on PEMEZ

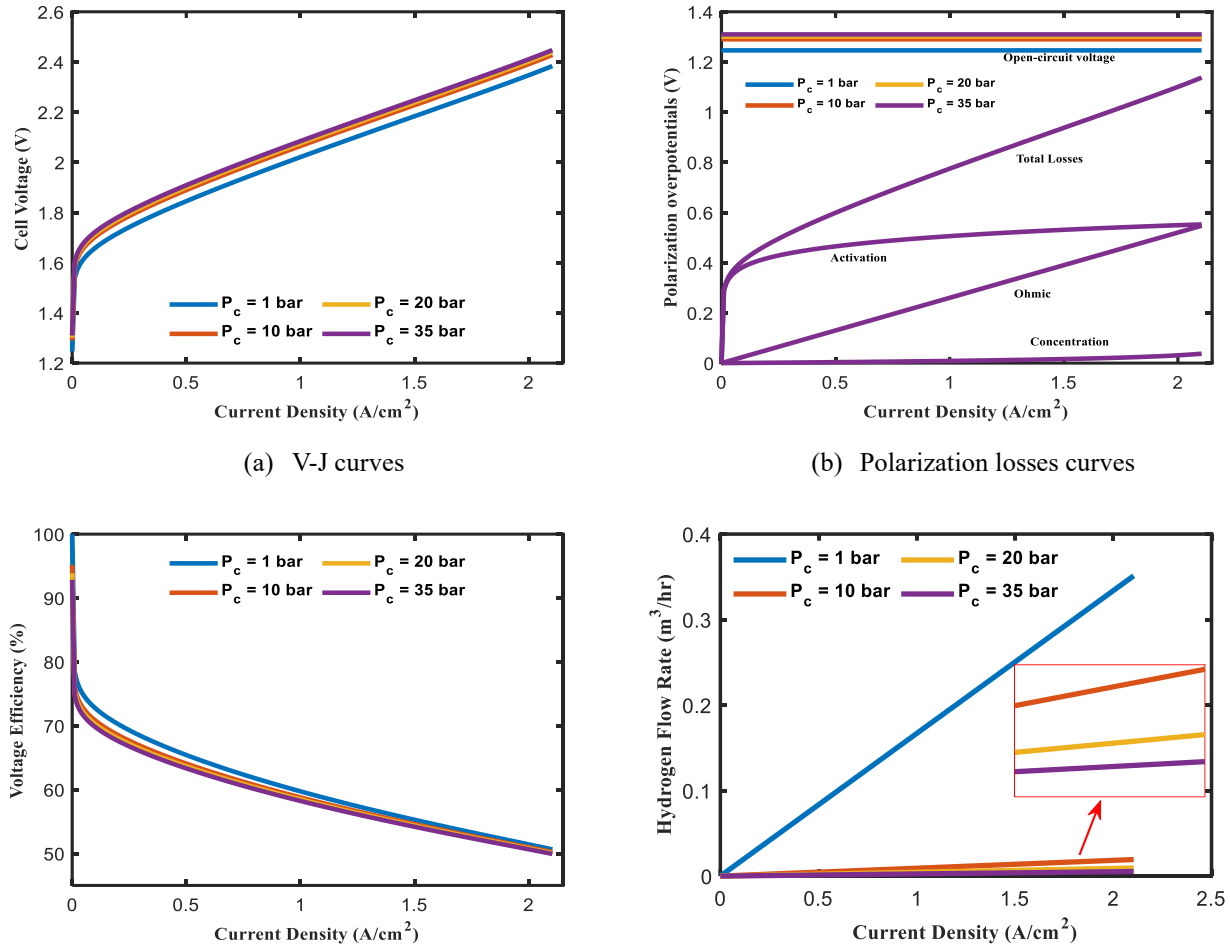

(a) V-J curves

(b) Polarization losses curves

(c) Voltage efficiency curves

(d) Hydrogen flow rate curves

Fig. 10. Effects of varying hydrogen pressure on PEMEZ

7.2. Dynamic simulation of hydrogen production

This subsection examines the dynamic behaviour of the PEMEZ in terms of hydrogen flow rate production in response to sudden changes in supplied current, while also considering operating temperature as an input. Notably, the measured hydrogen flow rate demonstrates a delayed response in reaching its steady-state value due to purification processes integrated with the PEMEZ stack. These processes, which include separators for removing water from hydrogen and hydrogen dryers, introduce a transient delay. Based on experimental observations of this behaviour, a dynamic model for hydrogen production can be established. A straightforward representation of this model assumes the hydrogen flow rate behaves as a first-order system, with parameters determined by measuring the time required for the flow rate to stabilize following a current step change. Fig. 11 describes the block diagram representation of the dynamic model, which is constructed in SIMULINK. The process begins by calculating the maximum theoretical hydrogen flow rate $M_{Hy,th}$ at a given current density and temperature using (13). Next, the steady-state hydrogen flow rate $M_{Hy,ss}$ is determined through (14)

and (15). Finally, the actual delayed hydrogen flow rate is derived by applying the first-order dynamic model, which captures the transient behaviour of the system.

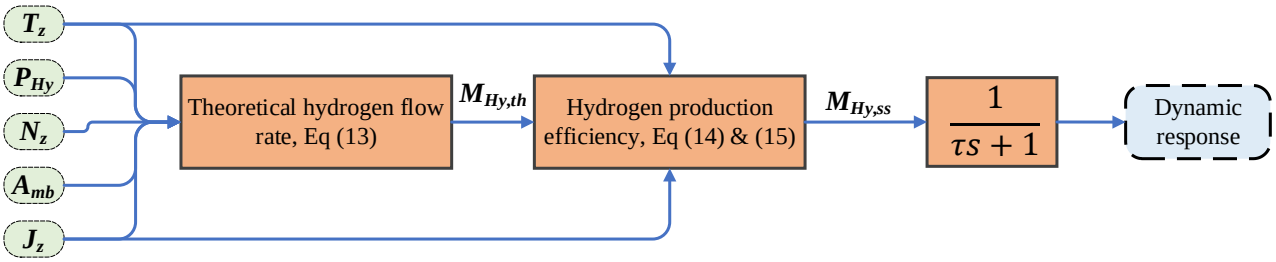

Fig. 11. Schematic block diagram of the dynamic model

It's worth highlighting that testcase (3) is employed here for the sake of understanding the dynamic nature of hydrogen production (refer to Section 2). Notably, the constants c_1, c_2, and c_3, which are crucial for determining hydrogen production efficiency, are empirically derived from experimental data as detailed in [46] (see Section 5.3). The numerical values of these constants are c_1=57.1081 %, c_2=-1699.6097e-04 A/cm^2, and c_3=1.0304 $A/(cm^2°C)$, respectively. In addition, the system's time constant τ for this testcase is approximately 5 s, according also to the experimental verifications.

In this context, current step changes of 10 A, 25 A, 50 A, and 35 A are introduced at 0 s, 50 s, 100 s, and 150 s, respectively, as illustrated in Fig. 12(a). These step variations are repeated for three operating temperatures (25 ℃, 35 ℃, and 50 ℃) while keeping both hydrogen and oxygen pressures constant at 1 bar. The corresponding PEMEZ hydrogen flow rate responses to these current and temperature variations are depicted in Fig. 12(b). From Fig. 12(b), it can be observed that the effect of temperature on the dynamic response of the hydrogen flow rate mirrors its impact on the steady-state response, as shown in Fig. 9(d). In both cases, a rise in temperature results in an increase in hydrogen production.

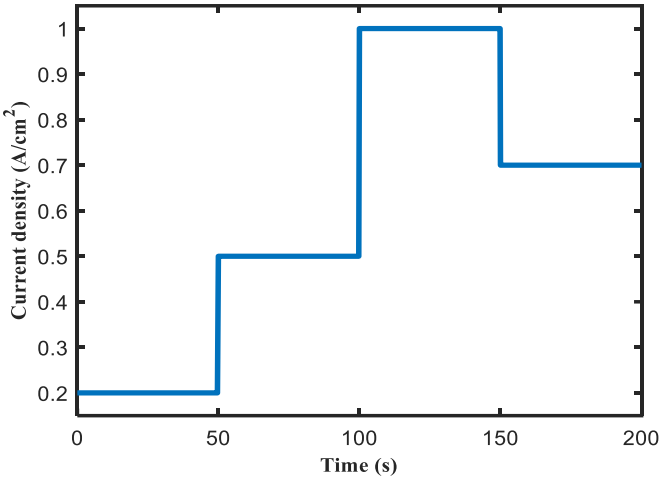

(a) Step variations on current density

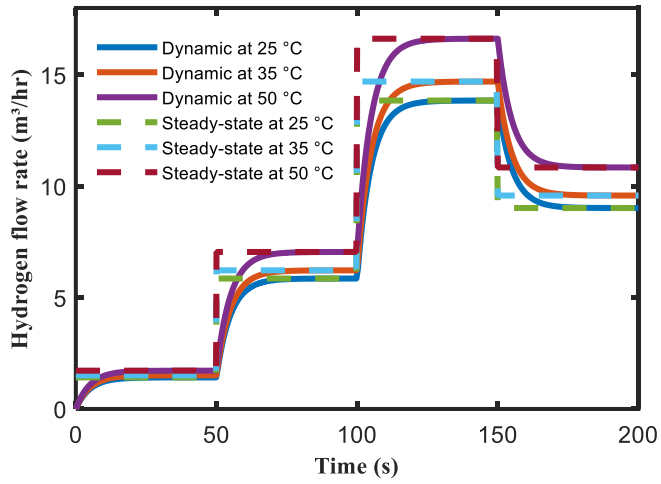

(b) Step response of hydrogen flow rate

Fig. 12. Dynamic response of PEMEZ hydrogen flow rate

8. Conclusion

The findings of this study underscore the potential of the WMVA as an effective tool for parameter estimation in the electrochemical modelling of PEMEZs. The proposed method demonstrated clear advantages over seven well-established optimization algorithms by achieving superior performance in terms of MSD, MAPD, and CEI. For instance, the minimum MAPD values recorded by WMVA were 0.05433% and 0.04905% for the two operation scenarios of the first testcase, 0.14297% and 0.28559% for the two operation scenarios of the second testcase, and 0.07835% for the third testcase, respectively. These results validate the WMVA's reliability and robustness across different testcases and operational conditions which signifies its precision for parameter estimation and enhanced PEMEZ modelling. Additionally, by examining the impact of temperature and hydrogen pressure on the steady-state performance, this work provides critical insights into the factors influencing PEMEZ behaviour. For

example, it has been proved that higher operating temperatures increase polarization losses at low current densities, while improving the polarization (J-V) curve at high current densities. The dynamic simulation further enriches these findings by illustrating how hydrogen production varies with temperature and current fluctuations. Overall, this research contributes to the development of more precise models for PEMEZ, which can lead to improved operational performance and more effective optimization strategies under diverse conditions.

Future work will include the development of a hardware-in-the-loop (HIL) testbed to validate the WMVA-based parameter estimation under real-time conditions, closing the loop between the proposed simulation model and an actual PEMEZ emulator. Beyond HIL integration, WMVA will be integrated into advanced real-time monitoring and control frameworks to enable adaptive optimization of operating conditions for maximized hydrogen production. The coupling between electrochemical model parameters and their collective impact on system efficiency will be investigated in depth. Multi-objective WMVA formulations, balancing energy efficiency against operational stability, will be explored, and degradation and aging effects will be incorporated to enhance the model's long-term predictive accuracy.

Data availability: Data are available from the authors upon reasonable request.

Declarations

Conflict of interest: The authors declare that there is no conflict of interest regarding the publication of this paper.

Ethical approval: This article does not contain any studies with human participants or animals performed by any of the authors.

Informed consent: Informed consent was obtained from all individual participants included in the study.

References

[1] R. Cozzolino, G. Bella. A review of electrolyzer-based systems providing grid ancillary services: current status, market, challenges and future directions. Frontiers in Energy Research. 12 (2024) 1358333.

[2] B. Kanouni, A.E. Badoud, S. Mekhilef, A. Elsanabary, M. Bajaj, I. Zaitsev. A fuzzy-predictive current control with real-time hardware for PEM fuel cell systems. Scientific Reports. 14 (2024) 27166.

[3] T. Mulo, P. Syam, A.B. Choudhury. Hybrid and Modified Harmony Search Optimization application in economic load dispatch with integrated renewable source. Electrical Engineering. 105 (2023) 1923-35.

[4] S. Bhattacharjee, V.S. Hiremath, D.M. Reddy, R.R. Mutra, N. Poornima. Prediction and analysis on the effects of different inlet diameters of a hydrogen gas tank during fast fill using ANN by the neurofit technique. Multiscale and Multidisciplinary Modeling, Experiments and Design. 8 (2025) 52.

[5] D. Kim, D. Yoon, S.H. Kim, T.W. Kim, Y.W. Suh. Sustainable Liquid-Organic-Hydrogen-Carrier-Based Hydrogen-Storage Technology Using Crude or Waste Feedstock/Hydrogen. Advanced Energy and Sustainability Research. 5 (2024) 2400177.
[6] A. Soleimani, S.H. Hosseini Dolatabadi, M. Heidari, A. Pinnarelli, B. Mehdizadeh Khorrami, Y. Luo, P. Vizza, G. Brusco. Progress in hydrogen fuel cell vehicles and up-and-coming technologies for eco-friendly transportation: an international assessment. Multiscale and Multidisciplinary Modeling, Experiments and Design. 7 (2024) 3153-72.
[7] J. Jin, Z. Wang, Y. Chen, C. Xie, F. Wu, Y. Wen. Modeling and energy management strategy of hybrid energy storage in islanded DC micro-grid. Electrical Engineering. 106 (2024) 6665-79.
[8] M. Awad, A. Said, M.H. Saad, A. Farouk, M.M. Mahmoud, M.S. Alshammari, M.L. Alghaythi, S.H.A. Aleem, A.Y. Abdelaziz, A.I. Omar. A review of water electrolysis for green hydrogen generation considering PV/wind/hybrid/hydropower/geothermal/tidal and wave/biogas energy systems, economic analysis, and its application. Alexandria Engineering Journal. 87 (2024) 213-39.
[9] R.A. Abdelsalam, M. Mohamed, H.E. Farag, E.F. El-Saadany. Green hydrogen production plants: A techno-economic review. Energy Conversion and Management. 319 (2024) 118907.
[10] V.M. Lopez, H. Ziar, J. Haverkort, M. Zeman, O. Isabella. Dynamic operation of water electrolyzers: A review for applications in photovoltaic systems integration. Renewable and Sustainable Energy Reviews. 182 (2023) 113407.
[11] X. Mao, Y. Tian, A. Yang, G. Zhang. Identification of Equivalent Circuit Parameters for Proton Exchange Membrane Electrolyzer (PEM) Engineering Models. IEEE Access. (2024).
[12] M. Koundi, H. El Fadil, Z. EL Idrissi, A. Lassioui, A. Intidam, T. Bouanou, S. Nady, A. Rachid. Investigation of hydrogen production system-based PEM EL: PEM EL modeling, DC/DC power converter, and controller design approaches. Clean Technologies. 5 (2023) 531-68.
[13] A.M. Abomazid, N.A. El-Taweel, F.H. EZ. Electrochemical optimization model for parameters identification of pem electrolyzer. 2020 IEEE Electric Power and Energy Conference (EPEC). IEEE2020. pp. 1-5.
[14] O. Atlam, M. Kolhe. Equivalent electrical model for a proton exchange membrane (PEM) electrolyser. Energy Conversion and management. 52 (2011) 2952-7.
[15] D. Guilbert, G. Vitale. Experimental validation of an equivalent dynamic electrical model for a proton exchange membrane electrolyzer. 2018 IEEE international conference on environment and electrical engineering and 2018 IEEE industrial and commercial power systems europe (EEEIC/I&CPS europe). IEEE2018. pp. 1-6.
[16] A. Awasthi, K. Scott, S. Basu. Dynamic modeling and simulation of a proton exchange membrane electrolyzer for hydrogen production. International journal of hydrogen energy. 36 (2011) 14779-86.
[17] M. Sartory, E. Wallnöfer-Ogris, P. Salman, T. Fellinger, M. Justl, A. Trattner, M. Klell. Theoretical and experimental analysis of an asymmetric high pressure PEM water electrolyser up to 155 bar. International Journal of Hydrogen Energy. 42 (2017) 30493-508.
[18] F.M. Nafchi, E. Afshari, E. Baniasadi, N. Javani. A parametric study of polymer membrane electrolyser performance, energy and exergy analyses. International Journal of Hydrogen Energy. 44 (2019) 18662-70.
[19] V. Ruuskanen, J. Koponen, K. Huoman, A. Kosonen, M. Niemelä, J. Ahola. PEM water electrolyzer model for a power-hardware-in-loop simulator. International Journal of Hydrogen Energy. 42 (2017) 10775-84.
[20] A.M. Abomazid, N.A. El-Taweel, H.E. Farag. Novel analytical approach for parameters identification of PEM electrolyzer. IEEE Transactions on Industrial Informatics. 18 (2021) 5870-81.
[21] Ø. Ulleberg. Modeling of advanced alkaline electrolyzers: a system simulation approach. International journal of hydrogen energy. 28 (2003) 21-33.
[22] D. Martinez, R. Zamora. Electrical implementations of an empirical electrolyser model for improved Matlab/Simulink simulations. International Journal of Renewable Energy Research. 9 (2019) 1060-70.
[23] M. Sánchez, E. Amores, L. Rodríguez, C. Clemente-Jul. Semi-empirical model and experimental validation for the performance evaluation of a 15 kW alkaline water electrolyzer. International Journal of Hydrogen Energy. 43 (2018) 20332-45.
[24] T. Yigit, O.F. Selamet. Mathematical modeling and dynamic Simulink simulation of high-pressure PEM electrolyzer system. International Journal of Hydrogen Energy. 41 (2016) 13901-14.

[25] S. Toghyani, S. Fakhradini, E. Afshari, E. Baniasadi, M.Y.A. Jamalabadi, M.S. Shadloo. Optimization of operating parameters of a polymer exchange membrane electrolyzer. International Journal of Hydrogen Energy. 44 (2019) 6403-14.
[26] M. Lebbal, S. Lecœuche. Identification and monitoring of a PEM electrolyser based on dynamical modelling. International journal of hydrogen energy. 34 (2009) 5992-9.
[27] K.W. Harrison, E. Hernández-Pacheco, M. Mann, H. Salehfar. Semiempirical model for determining PEM electrolyzer stack characteristics. (2006).
[28] A. Miró, C. Pozo, G. Guillén-Gosálbez, J.A. Egea, L. Jiménez. Deterministic global optimization algorithm based on outer approximation for the parameter estimation of nonlinear dynamic biological systems. BMC bioinformatics. 13 (2012) 1-12.
[29] B. Kanouni, A. Laib, S. Necaibia, A. Krama, J.M. Guerrero. Circulatory system-based optimization: A biologically inspired metaheuristic approach for accurately identifying a PEMFC's parameters. Energy Reports. 13 (2025) 4661-77.
[30] Z. Zhu, M. Zhu. A large domain identification problem in nonlinear systems using metaheuristics. Multiscale and Multidisciplinary Modeling, Experiments and Design. 7 (2024) 811-21.
[31] S. Das, P.C. Nayak, R.C. Prusty, S. Panda. Design of fractional order multistage controller for frequency control improvement of a multi-microgrid system using equilibrium optimizer. Multiscale and Multidisciplinary Modeling, Experiments and Design. 7 (2024) 1357-73.
[32] D. Izci, S. Ekinci, M. Altalhi, M.S. Daoud, H. Migdady, L. Abualigah. A new modified version of mountain gazelle optimization for parameter extraction of photovoltaic models. Electrical Engineering. 106 (2024) 6565-85.
[33] G. Liu, X. Tong, W. Ma, M. Zong, N. Zhang. A robust non-linear method for the state-of-health estimation for lithium-ion batteries based on dissipativity theory for electric vehicle applications. Multiscale and Multidisciplinary Modeling, Experiments and Design. 7 (2024) 2773-81.
[34] A.A. Dashtaki, S.M. Hakimi, E.S. Farahani, H. HassanzadehFard. Simultaneous optimal location and sizing of DGs in distribution system considering different types of MGs in an electricity market. Multiscale and Multidisciplinary Modeling, Experiments and Design. 7 (2024) 2443-59.
[35] R. Khajuria, P. Sharma, R. Kumar, R. Lamba, S. Raju. Efficient parameter extraction for accurate modeling of PEM fuel cell using Ali-Baba and forty thieves algorithm. Multiscale and Multidisciplinary Modeling, Experiments and Design. 8 (2025) 223.
[36] A. Laib, S. Necaibia, A. Krama, J.M. Guerrero. Pied kingfisher optimizer for accurate parameter extraction in proton exchange membrane fuel cell. Energy. 325 (2025) 136079.
[37] M. Espinosa-López, C. Darras, P. Poggi, R. Glises, P. Baucour, A. Rakotondrainibe, S. Besse, P. Serre-Combe. Modelling and experimental validation of a 46 kW PEM high pressure water electrolyzer. Renewable energy. 119 (2018) 160-73.
[38] R. Khajuria, R. Lamba, R. Kumar. Optimal parameter identification of pem electrolyzer using bald eagle search optimization algorithm. 2022 IEEE 10th Power India International Conference (PIICON). IEEE2022. pp. 1-6.
[39] R. Khajuria, R. Lamba, R. Kumar. Model Parameter Extraction for PEM Electrolyzer Using Honey Badger Algorithm. 2023 IEEE 3rd International Conference on Sustainable Energy and Future Electric Transportation (SEFET). IEEE2023. pp. 1-6.
[40] R. Khajuria, S. Yelisetti, R. Lamba, R. Kumar. Optimal model parameter estimation and performance analysis of PEM electrolyzer using modified honey badger algorithm. International Journal of Hydrogen Energy. 49 (2024) 238-59.
[41] B. Kanouni, A. Laib. Extracting accurate parameters from a proton exchange membrane fuel cell model using the differential evolution ameliorated meta-heuristics algorithm. Energies. 17 (2024) 2333.
[42] I. Ahmadianfar, A.A. Heidari, S. Noshadian, H. Chen, A.H. Gandomi. INFO: An efficient optimization algorithm based on weighted mean of vectors. Expert Systems with Applications. 195 (2022) 116516.
[43] B. Lekouaghet, M.A. Khelifa, A. Boukabou. Precise parameter estimation of PEM fuel cell via weighted mean of vectors optimizer. Journal of Computational Electronics. 23 (2024) 1039-48.

[44] W. Merrouche, B. Lekouaghet, E. Bouguenna, Y. Himeur. Parameter estimation of ECM model for Li-Ion battery using the weighted mean of vectors algorithm. Journal of Energy Storage. 76 (2024) 109891.
[45] M. Abdolhosseini, R. Abdollahi. Maximum Power Point Tracking Controller for Photovoltaic Systems Based on the Weighted Mean of Vectors Algorithm Optimization Algorithm under Partial Shading Conditions and Temperature Changes. Journal of Renewable Energy and Environment. 11 (2024) 81-7.
[46] R. García-Valverde, N. Espinosa, A. Urbina. Simple PEM water electrolyser model and experimental validation. international journal of hydrogen energy. 37 (2012) 1927-38.
[47] A.A.Z. Diab, A. Ezzat, A.E. Rafaat, K.A. Denis, H.A. Abdelsalam, A.M. Abdelhamid. Optimal identification of model parameters for PVs using equilibrium, coot bird and artificial ecosystem optimisation algorithms. IET Renewable Power Generation. 16 (2022) 2172-90.
[48] J. Lian, T. Zhu, L. Ma, X. Wu, A.A. Heidari, Y. Chen, H. Chen, G. Hui. The educational competition optimizer. International Journal of Systems Science. 55 (2024) 3185-222.
[49] H. Rezk, S. Ferahtia, A. Djeroui, A. Chouder, A. Houari, M. Machmoum, M.A. Abdelkareem. Optimal parameter estimation strategy of PEM fuel cell using gradient-based optimizer. Energy. 239 (2022) 122096.
[50] B. Abdollahzadeh, N. Khodadadi, S. Barshandeh, P. Trojovský, F.S. Gharehchopogh, E.-S.M. El-kenawy, L. Abualigah, S. Mirjalili. Puma optimizer (PO): A novel metaheuristic optimization algorithm and its application in machine learning. Cluster Computing. (2024) 1-49.
[51] S. Fu, K. Li, H. Huang, C. Ma, Q. Fan, Y. Zhu. Red-billed blue magpie optimizer: a novel metaheuristic algorithm for 2D/3D UAV path planning and engineering design problems. Artificial Intelligence Review. 57 (2024) 1-89.
[52] Y. Fu, D. Liu, J. Chen, L. He. Secretary bird optimization algorithm: a new metaheuristic for solving global optimization problems. Artificial Intelligence Review. 57 (2024) 1-102.
[53] F. Marangio, M. Santarelli, M. Calì. Theoretical model and experimental analysis of a high pressure PEM water electrolyser for hydrogen production. International journal of hydrogen energy. 34 (2009) 1143-58.
[54] F. Marangio, M. Pagani, M. Santarelli, M. Cali. Concept of a high pressure PEM electrolyser prototype. International Journal of Hydrogen Energy. 36 (2011) 7807-15.